

第 18 回 核燃焼プラズマ 統合コード研究会

18th Burning Plasma Simulation Initiative (BPSI) Meeting

日時：2020年12月17日(木)–18日(金)
場所：オンライン

(Ver. 1, 2021年3月2日発行)



合同会合

第 18 回核燃焼プラズマ統合コード研究会

18th Burning Plasma Simulation Initiative (BPSI) Meeting

および

核融合エネルギーフォーラムサブクラスター会合
シミュレーションクラスター 炉心プラズマモデリングサブクラスター
プラズマ物理クラスター 定常運転・制御サブクラスター

(Ver.1)

日時：2020年12月17日(木)–18日(金)

場所：オンライン開催

12月17日(木)

(13:00 – 17:00 ポスター講演 Poster presentation)

13:00 – 15:00 ポスター講演 1 Poster 1

コアタイム core time 13:00 – 14:00 Group 1A

14:00 – 15:00 Group 1B

15:00 – 17:00 ポスター講演 2 Poster 2

コアタイム core time 15:00 – 16:00 Group 2A

16:00 – 17:00 Group 2B

(開室 start 12:30、閉室 end 17:30)

12月18日(金)

9:30 – 9:35 事務連絡 Business announcement

(9:35 – 10:55 ポスター紹介 Poster talk)

(座長：糟谷)

9:35 – 9:55 講演 1-1 糟谷 (九大)

Development of integrated transport simulation scheme for impurity control in tokamak plasmas

9:55 – 10:15 講演 1-2 本多 (量研)

Coupling of EPED1 model to the integrated model GOTRESS+ and development of JT-60SA operation scenario

10:15 – 10:35 講演 1-3 森下 (京大)

Data assimilation system based on integrated transport simulation applying a reduced model of neutral beam injection heating

10:35 – 10:55 講演 1-4 登田 (核融合研)

Transport simulation directly coupled with gyrokinetic transport models for helical plasmas

10:55 – 11:15 休憩

(Session Leader : 村上)

11:15 – 12:00 議論 Discussion

12:00 – 13:00 昼休み

13:00 – 14:00 小グループ議論 Free discussion

(核融合エネルギーフォーラムサブクラスターとの合同会合)

14:00 – 14:10 藤田 (名大)

サブクラスター関係連絡事項 (定常運転・制御サブクラスターの世話人交代について)

14:10 – 14:40 宮戸 (量研)

IFERC 計算機シミュレーションセンターの現状報告

14:40 – 15:10 本多 (量研)

ITER に於ける統合モデリング活動関係の報告

15:10 – 15:40 花田 (九大)

日本の球状トカマクにおける EC によるプラズマ立上げ支援の研究 (ITPA 統合運転シナリオグループ活動への貢献)

15:40 – 16:00 休憩

16:00 – 16:30 若月 (量研)

ITPA 統合運転シナリオグループ活動報告

16:30 – 17:00 林 (量研)

サブクラスター活動に関する報告と今後の予定

17:00 散会

Poster number

18th BPSI meeting (2020)

Group 1A

P1A-1 登田慎一郎 (核融合研) S. Toda

Transport simulation directly coupled with gyrokinetic transport models for helical plasmas

P1A-2 鈴木航介 (京大) K. Suzuki

Fast-ion velocity-space reconstruction using FIDA measurements in LHD plasma

P1A-3 沼波政倫 (核融合研) M. Nunami

Visualization and similarity analysis for data of gyrokinetic simulations

P1A-4 成田絵美 (量研) E. Narita

Integrated transport simulations with a neural-network transport model and development of turbulence saturation rules

P1A-5 持永祥汰 (九大) S. Mochinaga

Transport analysis in PLATO tokamak using integrated code TASK

P1A-6 Apiwat Wisitsorasak (Mongkut's Univ. Tech. Thonburi)

Development of extended two-point model for asymmetric scrape-off layer

Group 1B

P1B-1 矢本昌平 (量研) S. Yamoto

Effects of impurity transport on detached divertor plasma transitions by time-dependent analysis of integrated divertor code SONIC

P1B-2 梅崎大介 (九大) D. Umezaki

Effect of large-angle elastic scattering between ions and neutral particles on density profile on divertor plate in divertor plasma

P1B-3 飯尾太那 (京大) D. Iio

Effect of magnetic fluctuations on the toroidal torque driven by electron cyclotron heating in tokamak plasmas

P1B-4 山本泰弘 (京大) Y. Yamamoto

Magnetic configuration and heating location dependences of the toroidal torques by ECH in LHD

P1B-5 Byung Jun Kang (SNU)

Gyrokinetic studies of fast ion precession driven drift instability in reversed shear burning plasmas

P1B-6 Yong Jik Kim (SNU)

Study of non-local transport events in flux-driven ITG turbulence

Group 2A

P2A-1 本多 充 (量研) M. Honda

Coupling of EPED1 model to the integrated model GOTRESS+ and development of JT-60SA operation scenario

P2A-2 福山 淳 (京大) A. Fukuyama

Progress of kinetic full wave analysis in plasmas

P2A-3 太田佳吾 (京大) K. Ota

Influence of the momentum dependence of radial diffusion on the transport of thermal and energetic particles in tokamak plasmas

P2A-4 佐々木真 (九大) M. Sasaki

Extraction of turbulent structures and quantification of energy transfer among structures by singular value decomposition

P2A-5 Taik Soo Hahm (SNU)

Bounce-kinetic studies on barely trapped particles' effect on trapped electron modes

P2A-6 糟谷直宏 (九大) N. Kasuya

Development of integrated transport simulation scheme for impurity control in tokamak plasmas

Group 2B

P2B-1 石田雅信 (九大) M. Ishida

Ion mass number dependence of resistant drift wave turbulence

P2B-2 石黒裕暉 (京大) Y. Ishiguro

Effects of toroidal field ripple on toroidal torque by electron cyclotron heating in JT-60U plasma

P2B-3 柳原洸太 (量研) K. Yanagihara

Development of ECCD calculation module for quasioptical ray tracing code

P2B-4 森下侑哉 (京大) Y. Morishita

Data assimilation system based on integrated transport simulation applying a reduced model of neutral beam injection heating

P2B-5 黒田 侑 (九大) Y. Kuroda

Evaluation of ballooning and kink instabilities in PLATO tokamak

P2B-6 庄司悠歩 (京大) Y. Shouji

Effects of anisotropic triton birth profile on triton burn-up ratio in LHD plasma

Transport simulation directly coupled with gyrokinetic transport models for adiabatic electron response for helical plasmas

S. Toda, M. Nunami, and H. Sugama

National Institute for Fusion Science, Oroshi-cho 322-6, Toki, Gifu, 509-5292, Japan

The quantitative prediction of the turbulent transport in toroidal plasmas is one of the most critical issues to be solved for realization of fusion energy. The gyrokinetic simulation for helical plasmas consumes much larger computer resources than those for tokamak plasmas, because the former requires a large number of mesh points along field lines to resolve helical ripple structures. Since it is still not easy to couple the nonlinear gyrokinetic simulation with an integrated transport simulation code for helical plasmas, the predictive model, which can quickly reproduce the nonlinear simulation results, is highly demanded. The heat diffusivity models for the electron and ion heat transport, and the quasilinear flux models for the particle and heat transport have been proposed to reproduce the nonlinear gyrokinetic simulation results in the kinetic electron condition for the ion temperature gradient (ITG) mode [1] in the Large Helical Device (LHD). These models are basically the functions of the linear simulation results, which are the linear growth rate and the characteristic quantity for the linear response of zonal flows. The heat diffusivity models have been installed into the transport code for simulating evolutions of the plasma profiles in the LHD when the additional modeling by R/L_{Ti} is used [2]. However, the particle diffusivity cannot be modeled for the hollow and flattened density profiles, which are typical in the LHD experimental results [2]. Furthermore, the quasilinear flux model is not directly coupled with the transport simulation so far, because the used quasilinear flux model depends on the cross-phase between the fluctuating potential and temperature (or the density) and it is considered that this cross-phase term cannot be modeled by the temperature or density gradients.

In this study, the reduced model [3] for the ion heat diffusivity in the adiabatic electron condition is directly coupled with the transport simulation by performing the GKV [4] linear simulation. The linear growth rate is evaluated at each time step in the transport simulation. The zonal flow decay time, which is characteristic for the linear response of zonal flows, is dynamically set as the initial state in the transport simulation. The neoclassical diffusion coefficient is derived from DGN/LHD database with the low- β limit ($\beta = 0$). The reduced model for the ion heat diffusivity is shown as

$$\frac{\chi_i^{\text{model}}}{\chi_i^{\text{GB}}} = \frac{A_{1,\text{ad}} \mathcal{L}^{\alpha_{\text{ad}}}}{A_{2,\text{ad}} + \tilde{\tau}_{\text{ZF}} / \mathcal{L}^{1/2}}, \quad (1)$$

where $\chi_i^{\text{GB}} (= \rho_i^2 v_{ti} / R)$ is the gyro-Bohm diffusivity and $\mathcal{L} \left(\equiv \int (\tilde{\gamma}_{\tilde{k}_y} / \tilde{k}_y^2) d\tilde{k}_y \right)$ is the quantity related with the mixing length estimate. Here, $\tilde{\gamma}_{\tilde{k}_y} (= \gamma_{\tilde{k}_y} / (v_{ti} / R))$ is the normalized linear growth rate of the ITG mode. The coefficient is given by $A_{1,\text{ad}} = 1.8 \times 10$, $A_{2,\text{ad}} = 5.2 \times 10^{-1}$ and $\alpha_{\text{ad}} = 0.38$. The linear zonal flow response function is defined by $\mathcal{R}_{\tilde{k}_x}(t) \equiv \left\langle \tilde{\phi}_{\tilde{k}_x, \tilde{k}_y=0}(t) \right\rangle / \left\langle \tilde{\phi}_{\tilde{k}_x, \tilde{k}_y=0}(t=0) \right\rangle$. Note that the zonal flow response function for $\tilde{k}_x = 0.25$ is used to evaluate the representative values of the zonal flow decay time, because there are peaks of the wavenumber spectra around $\tilde{k}_x = 0.25$

in the nonlinear simulation results. The zonal flow decay time is defined by $\tau_{ZF} \equiv \int_0^{\tau_f} dt \mathcal{R}_{\tilde{k}_x}(t)$, where the upper limit τ_f in the integral is set to be $\tau_f = 25R/v_{ti}$ in the adiabatic electron condition for modeling the diffusivities or fluxes. The correlation time of the turbulent sources is shorter than $25R/v_{ti}$. Therefore, the zonal flow response function for $\tau_f > 25R/v_{ti}$ is not considered to influence the generated zonal flow level. The normalized zonal flow decay time is defined as $\tilde{\tau}_{ZF} = \tau_{ZF}/(R/v_{ti})$.

The simulation result for the adiabatic electron response of the stationary ion temperature profile can be obtained. The linear growth rate is calculated by the GKV at each time step in the dynamical transport simulation by TASK3D and the value of the ion heat diffusivity is obtained. In the adiabatic electron condition, the simulation result for the T_i profile show the good agreement with the experimental result. The stationary profiles of the turbulent and neoclassical diffusivities are studied. The ITG mode is destabilized in the radial region $0.20 < \rho < 0.80$. The turbulent transport is dominant compared with the neoclassical transport in the radial region $0.20 < \rho < 0.80$, where the positive electric field is chosen. The transport simulation results for the ion temperature profiles coupled with the reduced model are compared and have the good agreement with those for the additional modeling of the linear growth rate by R/L_{T_i} .

This work is partly supported by the NIFS Collaboration Research Programs, NIFS20KNST168 (Plasma Simulator) and the Collaborative Research Program of Research Institute for Applied Mechanics, Kyushu University, 2020FP-11.

- [1] S. Toda et al., Phys. Plasmas **26**, 012510 (2019).
- [2] S. Toda et al., Journal of Physics: Conference Series **561**, 012020 (2014).
- [3] M. Nunami, T. -H. Watanabe and H. Sugama, Phys. Plasmas **20**, 092307 (2013).
- [4] T. -H. Watanabe and H. Sugama, Nucl. Fusion **46**, 24 (2006).

Visualization and similarity analysis for data of gyrokinetic simulations

Shuta Kitazawa¹ and Masanori Nunami²

¹*Nagoya University, Nagoya 464-8601, Japan,*

²*National Institute for Fusion Science, Toki 509-5292, Japan*

The gyrokinetic simulation is a powerful tool to analyze the turbulent transport of the magnetically confined plasmas. However, since the data obtained from the gyrokinetic simulations consist of time series of five-dimensional distribution functions, it is difficult to fully capture the physics in the turbulent transport phenomena. While the direct visualization of the distribution function has been quite important for the intuitive analysis for the phenomena, in this work, a novel visualization tool and a novel data analysis way for the GK simulation data are developed with the aid of the latest visualization and data science techniques. Since the developed way enables us to visualize the higher-dimensional data in the virtual space and to capture the characteristic structure of the distribution functions, it becomes easy to analyze the complicated the gyrokinetic simulation data.

1 Introduction

In magnetically confined fusion plasma researches, the gyrokinetic simulation is a reliable way to predict the turbulent transport. In the last decade, it becomes possible to validate the gyrokinetic simulation results against the experimental observations, and to predict the profiles of the plasma temperature and density by performing the simulations with changing the input parameters of the plasma profiles [1]. Since the gyrokinetic simulation can treat the evolutions of the distribution function in five-dimensional (5D) phase space, we can obtain full data of the time-series of 5D distribution functions. On the other hand, it is quite difficult to fully capture the physics in the simulation data because of the hugeness of the 5D data. Therefore, the direct visualization and development of the data analysis scheme for the 5D distribution functions obtained from the gyrokinetic simulations are significant and strongly demanded for understandings of the turbulent transport physics in the magnetized plasmas. In this work, we develop a novel visualization tool and a novel data analysis scheme using the latest techniques for the visualization and data science. Using the developed schemes, it may be possible to analyze the complicated the gyrokinetic simulation data more intuitively.

author's e-mail: nunami.masanori@nifs.ac.jp

2 Mapping of velocity distribution function into wavenumber space

In our previous work [2], we developed the visualization tool for the gyrokinetic simulation data using the head mounted display (HMD) which is a display device with small display optic in front of each eye, and the Unity [3] which is a cross-platform game engine. The developed tool enables us to visualize the data of 5D distribution functions from the gyrokinetic simulations in 3D real-space with 2D velocity-space distribution functions obtained by the gyrokinetic code, GKV [4]. However, if we have performed it without any reduction of the simulation data for 5D distribution functions, it is extremely hard to visualize them for the sake of the hugeness of the data. Therefore, in actuality, we cannot fully capture the physics in the simulation data by the conventional way. In order to reduce the file size of the distribution function data for the visualization, we employ the image data for the 2D velocity-space part of the 5D distribution function data, because the image data is lighter than the full data of the distribution functions. Then we collect whole images of the 2D velocity-space part of the distribution function data at each position in 3D real-space, and map the image into the 3D real-space. Using the mapping data, we are able to visualize the data of 5D distribution functions with quite light load. The figure 1 shows an example of the visualization, and we can plot the mapping of 2D velocity-space distribution functions into the 2D space (k_x, k_y) which is the wavenumber space perpendicular to the magnetic field at fixed the remaining real-space coordinate z . In the figure, in addition to the 2D velocity-space structures of the distribution functions, we can easily find that there exists the certain global structures in higher dimensional phase space.

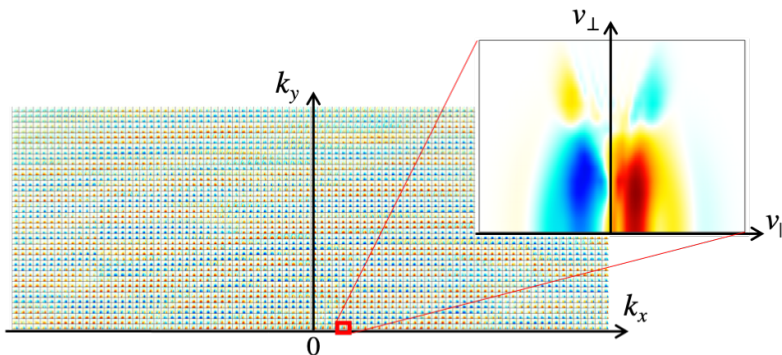


Fig. 1 Mapping of velocity-space distribution functions into wavenumber space. At each position in wavenumber space, the corresponding velocity-space distribution functions obtained by the gyrokinetic simulation are fully mapped.

3 Similarity analysis

Using the mapping data of the distribution functions obtained in the previous section, we perform the similarity analysis to extract the features of the distribution functions from the gyrokinetic simulations. In the analysis, we employ the numerical library, OpenCV [5], which is a library of programming functions mainly aimed at real-time computer vision. Here, we focus on the data of the turbulence simulations for the “inward-shifted” case of the LHD [6] plasma that has an important feature, i.e., the enhanced zonal flows which cause the plasma transport reduction. For the mapping data, we find that there exists robust structures in the distribution functions in the wavenumber region where the zonal flows are most enhanced. In the region, there exists anti-symmetrical structures for v_{\parallel} -direction, and V-shaped structure for v_{\parallel} - v_{\perp} space. Therefore, we regard such characteristic structures as a reference structure of the distribution functions, and find the similarities in whole mapping data using similarity analysis functions in OpenCV library including the feature detection technique, AKAZE [7]. The AKAZE is the accelerated version of KAZE [8] which is a 2D feature detection and description method that operates completely in a nonlinear scale space. Using the function, we can detect similarities of structure to the reference structure in the zonal-flow enhanced region with the anti-symmetrical structures for v_{\parallel} -direction and the V-shaped structure for v_{\parallel} - v_{\perp} space. And we find that the similarities remains for long simulation time. This means that it may be possible to extract the important region in the gyrokinetic simulations at an early simulation phase.

4 Summary

The schemes to visualize and analyze the gyrokinetic simulation data of the distribution functions in 5D phase space have been newly developed. By employing the image data for 2D velocity-space distribution functions instead of the full data of 5D distribution functions, and mapping the image into the remaining 3D space with the wavenumber space, we can visualize the data of the distribution functions with quite light load. Using the mapping visualization, furthermore, we can extract the characteristic structures of the distribution functions by means of the similarity analysis.

Acknowledgment

This work is supported in part by the RIAM collaborative Research Program (2020FP-1), NIFS Collaborative Research Program (NIFS20KNST161), and JSPS KAKENHI (20K03907). The simulations were performed by using JFRS-1 at IFERC CSC (GDKTHEL) and “Plasma Simulator” at NIFS.

[1] T. Görler, *et al.*, Phys. Plasmas **21**, 122307 (2014).

[2] S. Kitazawa, M. Nunami, *et al.*, The 81st national convention of IPSJ, 2M-05, Fukuoka, Japan (2019).

18th Burning Plasma Simulation Initiative (BPSI) Meeting

- [3] Unity official web site, <https://unity.com/> .
- [4] T.-H. Watanabe and H. Sugama, Nucl. Fusion **46**, 24 (2006).
- [5] OpenCV official web site, <https://opencv.org/> .
- [6] Y. Takeiri, *et al.*, Nucl. Fusion **57**, 102023 (2017).
- [7] P. F. Alcantarilla, J. Nuevo, and A. Bartoli, *Fast Explicit Diffusion for Accelerated Features in Nonlinear Scale Spaces*, British Machine Vision Conf. (BMVC), Bristol, UK (2013).
- [8] P. F. Alcantarilla, A. Bartoli, and A. J. Davison, *KAZE Features*, Eur. Conf. on Computer Vision (ECCV), Firenze, Italy (2012).

Integrated transport simulations with a neural-network transport model and development of turbulence saturation rules

E. Narita¹, M. Honda¹, M. Nakata^{2,3}, M. Yoshida¹ and N. Hayashi¹

¹National Institutes for Quantum and Radiological Science and Technology, Naka, Ibaraki 311-0193, Japan

²National Institute for Fusion Science, Toki, Gifu 509-5292, Japan

³The Graduate University for Advanced Studies, Toki, Gifu 509-5292, Japan

1 Introduction

Since density and temperature profiles severely affect fusion power, accurate predictions of these profiles are required. The gyrokinetic-based turbulent transport models, such as TGLF [1] have been found to give reasonable agreement with experiments, but introducing the detailed descriptions of turbulence physics has tended to increase the computational cost. To accelerate the profile predictions, a neural-network (NN) based approach has been undertaken (see e.g., [2–4]). Our study is also developing a NN based turbulent transport model DeKANIS based on a combination of the gyrokinetic code GKW [5] and JT-60U experimental data. DeKANIS has originally been developed for particle transport [6], and then it has extended to cover both particle and heat transport [7]. Since the previous model was hard to perform stable simulations with integrated codes, the NN model has been improved. Furthermore, the prediction capabilities of two different turbulent saturation models adopted in DeKANIS have been checked using JT-60U and JET plasmas.

2 Improvements on the NN model for integrated simulations

DeKANIS predicts turbulent particle and heat fluxes for electrons in a quasilinear limit as $\bar{\Gamma}_e = \bar{D} \left(\frac{R}{L_{n_e}} + C_T \frac{R}{L_{T_e}} + C_P \right)$ and $\bar{Q}_e = \bar{\chi}_e \left(C_N \frac{R}{L_{n_e}} + \frac{R}{L_{T_e}} + C_{HP} \right)$, respectively. Here, non-dimensional \bar{D} , $\bar{\chi}$, R/L_n and R/L_T are the particle and heat diffusivities in proportion to fluctuation amplitudes and the density and temperature gradients, respectively. The fluxes are composed of the diagonal (diffusion) and off-diagonal (convection) terms, which are quantitatively determined by calculating the off-diagonal-term coefficients ($C_{T,P,N,HP}$) and the diffusivities (\bar{D} and $\bar{\chi}_e$). Note that the relationship between $C_{T,N}$, \bar{D} , and $\bar{\chi}_e$ satisfies the Onsager symmetry. Predicting diagonal and off-diagonal terms individually could be helpful to understand the effects of the transport processes on density and temperature profile formation. In addition to the electron fluxes, DeKANIS also predicts the ion heat flux, which is given as $\bar{Q}_i = \frac{\bar{\chi}_{i,\text{eff}}}{\bar{\chi}_{e,\text{eff}}} \bar{\chi}_{e,\text{eff}} \frac{R}{L_{T_i}} \frac{n_i}{n_e} \frac{T_i}{T_e}$. Here, $\bar{\chi}_{\text{eff}}$ is the normalized effective heat diffusivity, which is defined when the heat flux is expressed with only the diagonal term. If \bar{Q}_e is given, \bar{Q}_i can be calculated by determining $\bar{\chi}_{i,\text{eff}}/\bar{\chi}_{e,\text{eff}}$.

DeKANIS estimates $C_{T,P,N,HP}$, \bar{D} , $\bar{\chi}_e$ and $\bar{\chi}_{i,\text{eff}}/\bar{\chi}_{e,\text{eff}}$ with a fully-connected feed-forward NN model. The training dataset for the NN construction has been developed with 23 JT-60U H-mode plasmas. The values of $C_{T,P,N,HP}$ and $\bar{\chi}_{i,\text{eff}}/\bar{\chi}_{e,\text{eff}}$ have been given by GKW linear calculations.

On the other hand, \bar{D} has been determined by the two different saturation models. The first model calculates \bar{D} to match it to the the experimental turbulent particle flux. The case using the first model is referred to as DeKANIS-1. The second model related to DeKANIS-2 will be shown in later. The NN model has been constructed to reproduce the training dataset. Here, the inputs are 12 plasma parameters, such as R/L_{n_e} and R/L_{T_e} , and the outputs are the six coefficients: $C_{T,P,N,HP}$, \bar{D} and $\bar{\chi}_{i,\text{eff}}/\bar{\chi}_{e,\text{eff}}$. After obtaining the coefficients, DeKANIS computes $\bar{\chi}_e$ not to break the Onsager symmetry.

The training dataset has been prepared in the same way as the previous DeKANIS [7], but the number of the data points has increased from 2,232 to 7,268. As for the hyperparameters of the NN model, the number of hidden layers and units has been determined using Bayesian optimization with a Python library Hyperopt [8,9] through a Keras wrapper Hyperas [10], whereas it was optimized manually for the previous model. Furthermore, the activation function of the output layer has changed from the linear function to the softsign one to limit outputs within three standard deviations of the average in the training data. Setting the upper and lower limits prevents unreasonable extrapolation, which can cause unstable transport simulations.

Due to the aforementioned modifications, DeKANIS-1 has realized the density and temperature profile predictions using the integrated code

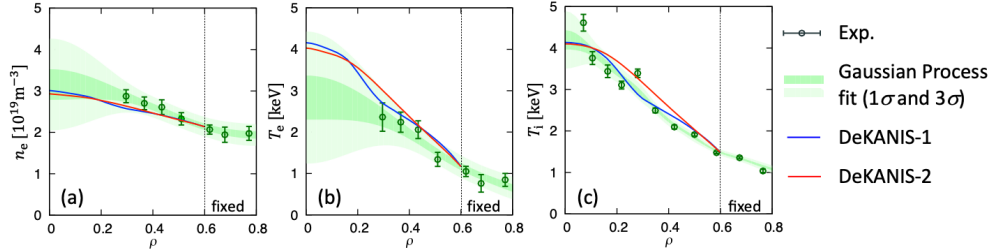


Figure 1. Radial profiles of (a) the electron density and the (b) electron and (c) ion temperatures predicted by DeKANIS-1 (blue) and -2 (red) using TOPICS for a JT-60U plasma outside the training dataset.

TOPICS [11]. Figure 1 demonstrates that DeKANIS-1 works for a JT-60U H-mode plasma that is not included in the training dataset. It takes about three hours to obtain the steady-state profiles with a single core, which is much faster than the conventional models like TGLF.

3 A theory based turbulence saturation model for applicability to a wide range of plasma parameters

As the first saturation model directly uses the experimental value, DeKANIS-1 is pragmatic in the known parameter range. However, it is difficult to use outside the known parameter range. The second saturation model has

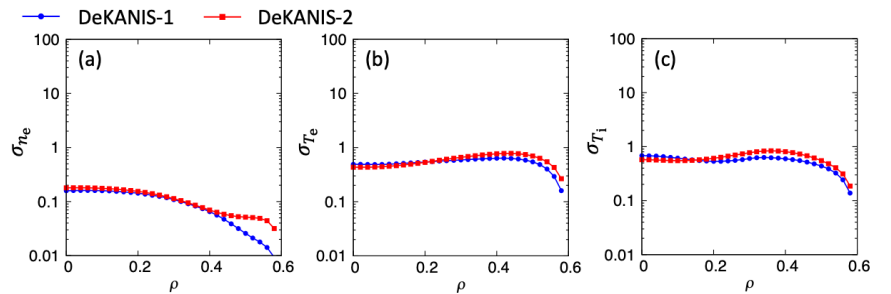


Figure 2. The root-mean-square errors σ of the (a) electron density and the (b) electron and (c) ion temperatures predicted by DeKANIS-1 (blue) and -2 (red) using TOPICS for 14 JT-60U test cases at each radial point.

been introduced to apply DeKANIS to devices other than JT-60U. It is based on the mixing-length theory, assuming that \bar{D} can be expressed by the quasilinear diffusivity $\bar{\gamma}/\bar{k}_\theta^2$ and the residual zonal flow level \mathcal{L}_{ZF} [12]: $\bar{D} = 1.86 \times 10^{-4} (\bar{\gamma}/\bar{k}_\theta^2)^{1.5} L_{ZF}^{-2.71}$. To use the scaling formula, the other NN model has been constructed for DeKANIS-2 to reproduce $\bar{\gamma}/\bar{k}_\theta^2$ and \mathcal{L}_{ZF} that have been calculated by GWK. As the NN model of DeKANIS-2 does not need to output \bar{D} , it is free from the experimental values. The modifications made for the DeKANIS-1's NN model have also been performed for the DeKANIS-2's. The prediction results from DeKANIS-2 for the JT-60U H-mode plasma are similar to those from DeKANIS-1 (figure 1), and it has been found that the the root-mean-square errors σ of the their results for the 14 test cases are at the similar level (figure 2). Here, σ of ξ is given as $\sigma_\xi = \sqrt{\frac{1}{N} \sum (\xi_{\text{sim}}/\xi_{\text{exp}} - 1)^2}$, where $\xi_{\text{sim}(\text{exp})}$ is the simulated (experimental) value of ξ , and N is the number of the data points.

The two DeKANIS models have been applied to JET plasmas, whose data have been taken from the ITPA International Multi-Tokamak Profile Database [13]. We have estimated $\bar{\Gamma}_e$, \bar{Q}_e and \bar{Q}_i for 16 L- and H-mode plasmas, and evaluated

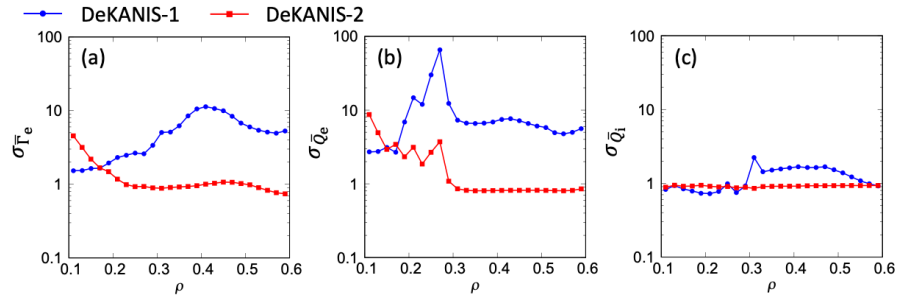


Figure 3. The root-mean-square errors σ of the (a) electron density and the (b) electron and (c) ion temperatures predicted by DeKANIS-1 (blue) and -2 (red) using TOPICS for 16 JET plasmas at each radial point.

σ , as shown in figure 3. It can be found that DeKANIS-2 gives better predictions, though the accuracy is worse than that for JT-60U. Since the accuracy of DeKANIS-2 can be improved by replacing the mixing-length-like scaling formula with another one, the saturation model will be updated near future.

References

- [1] G.M. Staebler *et al.*, Phys. Plasmas **12** 102508 (2005).
- [2] M. Honda and E. Narita, Phys. Plasmas **26** 102307 (2019).
- [3] O. Meneghini *et al.*, Nucl. Fusion **57** 086034 (2017).
- [4] K.L. van de Plassche *et al.*, Phys. Plasmas **27** 022310 (2020).
- [5] A.G. Peeters *et al.*, Comput. Phys. Commun. **180** 2650 (2009).
- [6] E. Narita *et al.*, Nucl. Fusion **59** 106018 (2019).
- [7] E. Narita *et al.*, Proceedings of 17th Burning Plasma Simulation Initiative Meeting (2019).
- [8] J. Bergstra *et al.*, Proceedings of the 30th International Conference on Machine Learning, **28** (2013).
- [9] <http://jaberg.github.io/hyperopt/>
- [10] <http://maxpumperla.com/hyperas/>
- [11] N. Hayashi and JT-60 Team, Phys. Plasmas **17** 056112 (2010).
- [12] E. Narita *et al.*, Plasma Phys. Controlled Fusion **60** 025027 (2018).
- [13] The ITER 1D Modelling Working Group, Nucl. Fusion **40** 1955 (2000).

Transport analysis in PLATO tokamak using integrated code TASK

S. Mochinaga¹⁾, N. Kasuya^{1,2)}, A. Fukuyama³⁾,
Y. Nagashima^{1,2)} and A. Fujisawa^{1,2)}

¹⁾ IGES, Kyushu University, ²⁾ RIAM, Kyushu University, ³⁾ Kyoto University

1. Introduction

PLATO device at Kyushu University is a tokamak to observe detailed spatio-temporal structure of plasma turbulence with several diagnostics, as tomography systems with more than 1500 detectors and three HIBPs [1,2]. The PLATO device is designed to have plasma parameters as major radius $R = 0.7$ m, minor radius $a = 0.2$ m, plasma current $I_p = 40$ kA, electron temperature $T_e = 0.2$ keV, and density $n = 1.0 \times 10^{19}$ m⁻³. A number of integrated codes have been developed, and are applied to evaluation of performance of several tokamak plasmas [3-5]. This paper presents transport analyses using the integrated simulation code TASK (Transport Analysis System for tokamak) [6] to predict experimental conditions. TASK code has a modular structure, which includes various functions to calculate particle and heat transport, equilibrium, wave heating, etc. A self-consistent simulation is realized by modules selected in accordance with the research purpose, which are coupled with a data exchange interface. In the simulation of magnetically-confined plasmas, transport calculation is performed under the assumption that plasma is in the MagnetoHydroDynamics (MHD) equilibrium state. Conventional transport analyses with TASK code have been carried out by using a fixed-boundary two-dimensional equilibrium code, TASK/EQ, and a one-dimensional transport code, TASK/TR. It is important to consider the external coil conditions to represent more realistic experimental situations in PLATO. Therefore, in this study, we have developed a routine to include a free-boundary two-dimensional equilibrium code TASK/EQU, which calculates the plasma equilibrium with vertical field coils, to analyze transport in PLATO plasmas. TASK/EQU code has been also used for the analyses of MHD instabilities in PLATO [7]. The developed transport analysis routine is used to predict the plasma performance, and dependences on parameters that are externally controllable in experiments are evaluated. PLATO device is no direct heating tools for ions, so is investigated how to improve ion temperature by power balance analysis in transport processes.

2. Transport analysis model

Time evolutions of plasma quantities are obtained by coupling equilibrium and transport calculations. In the equilibrium calculation, the following Grad-Shafranov equation is solved.

$$\nabla \cdot \frac{1}{R^2} \nabla \psi = -4\pi^2 \mu_0 \frac{dp}{d\psi} - \frac{I}{R^2} \frac{dI}{d\psi}. \quad (1)$$

Here, ψ , p , I , R , μ_0 are the poloidal flux function, the plasma pressure, the poloidal current, the major radius, and the permeability, respectively. In the free-boundary equilibrium calculation, ψ includes contributions both from the plasma current ψ_p and the external vertical coil current ψ_{coil}^i as $\psi = \psi_p + \sum_i \psi_{coil}^i$, where i is the index number of the coils.

In the transport calculation, the following particle and heat transport equations are solved for plasma species s .

$$\frac{1}{V'} \frac{\partial}{\partial t} (n_s V') = -\frac{1}{V'} \frac{\partial (V' \Gamma_s)}{\partial \rho} + S_s, \quad (2)$$

$$\frac{1}{V'^{5/3}} \frac{\partial}{\partial t} \left(\frac{3}{2} n_s T_s V'^{5/3} \right) = -\frac{1}{V'} \frac{\partial (V' Q_s)}{\partial \rho} + P_s, \quad (3)$$

Here, n_s , T_s , S_s , P_s , ρ are the plasma density, the plasma temperature, the particle source, the heat source, the normalized minor radius, respectively, and $V' = dV/d\rho$ is the radial derivative of plasma volume. The heat sources for electron and ion are given by

$$P_e = P_{OH} - P_{EQ}, \quad (4)$$

$$P_i = P_{EQ}, \quad (5)$$

where P_{OH} is the ohmic heating power expressed as

$$P_{OH} = \eta j^2, \quad (6)$$

and P_{EQ} is the collisional energy transfer from electrons to ions expressed as

$$P_{EQ} = \frac{3}{2} n \frac{T_e - T_i}{\tau_{ei}}, \quad (7)$$

Here η is the plasma resistivity, j is the plasma current density, and

$$\tau_{ei} = \frac{3\sqrt{2}\pi^{1.5}\epsilon_0^2 m_e m_i}{ne^4 Z_e Z_i \ln\Lambda} \left(\frac{T_e}{m_e} + \frac{T_i}{m_i} \right)^{1.5} \quad (8)$$

is the electron-ion collision time. In the particle transport equation, the quasi-neutrality condition is assumed. Transport coefficients includes neoclassical and turbulent contributions. For the neoclassical transport model, NCLASS [8] is used to obtain the diffusion coefficients and convection velocities of particles and heat. The plasma resistivity is also obtained by using NCLASS. For the turbulent transport model, the CDBM model [9] is used to obtain the thermal diffusivity. The transport coefficients are the sum of the neoclassical and turbulent thermal diffusion coefficients.

We have developed a scheme for linking equilibrium module EQU and transport module TR. The TASK/TOT module is used to control the time evolution of the modules. In the equilibrium and transport linkage scheme, each module exchanges data via data interface BPSD. Quantities regarding to the plasma shape, metric and magnetic-surface averages are obtained from the equilibrium calculations, and are used in the transport calculations. On the other hand, in the equilibrium calculation, the pressure profile obtained from the transport calculation is used as an initial condition, and the poloidal current profile is derived from the safety factor q in the right-hand side of Eq. (1). In this study, change of the current distribution on the flat-top of PLATO plasma discharges is considered to be small and is not reconstructed in the evolution.

3. Transport analysis with PLATO parameter

The developed scheme (EQU-TR combination) is used to evaluate the plasma performance and transport property with PLATO plasma parameters. Toroidal magnetic field $B_t = 0.3$ T and plasma current $I_p = 40$ kA are kept to be constant, and the density at the plasma center is set to be $n_0 = 1.0 \times 10^{19} \text{ m}^{-3}$ by supplying particles from the edge of the plasma as particle supply with the gas-puffing method. PLATO device has main three pairs of vertical field coils; D (dipole), Q (quadropole), and H (hexapole) coils, and two pairs of feedback coils; F1 and F2 coils. Ohmic heating coil in the center solenoid is divided into two pairs; OH and OHC coils as in Fig. 1 [10]. In this calculation, only D, Q and H coils are considered for control. Figure 1 shows the poloidal cross-section of the flux contours of the equilibrium with EQU calculation.

The obtained equilibrium has $R = 0.7$ m, $a = 0.18$ m, ellipticity $\kappa = 1.9$, and triangularity $\delta = 0.4$. The plasma profiles in the steady-state are obtained with TR calculation as in Fig. 2. The obtained temperature has $T_e = 130$ eV and $T_i = 35$ eV at the center. The conventional transport analysis method (EQ-TR combination) is also carried out using the same shaping parameters. Similar results are obtained both with EQ and EQU, but the electron temperature in the EQU-TR case is lower than the EQ-TR case, because the ohmic heating power near the center of the plasma is different as in Fig. 2(d). The current profile is radially broader in the EQU case, so the current is smaller near the center with restriction of the same total plasma current. In this calculation, the neoclassical convection directs inward, but contribution of the diffusion is much larger. The turbulent diffusion is dominant except near the center, where the density and temperature profiles are flat.

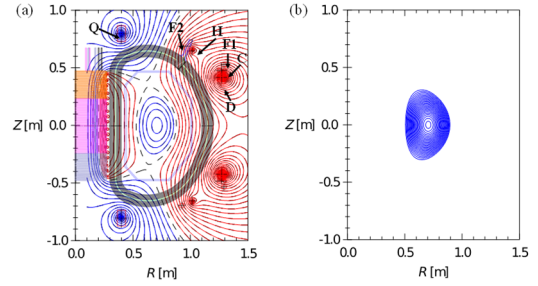


Fig.1. Equilibrium magnetic configuration of PLATO tokamak obtained by (a)TASK/EQU and (b)TASK/EQ. The position of each vertical field coils and the ohmic coils are also shown.

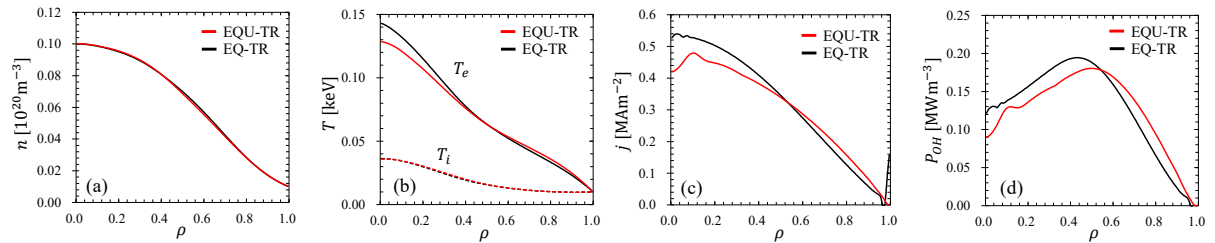


Fig.2. Radial profiles of (a) density, (b) electron and ion temperature, (c) current density, (d) ohmic heating power. The cases with EQU-TR and EQ-TR are shown.

4. Dependences on externally controllable quantities

The dependence on the particle feeding rate is evaluated, as it is externally controllable in PLATO experiments. The plasma parameters and coil currents are same with those in the previous section. The particle feeding rate is adjusted to give the density at the center from $n_0 = 0.5$ to $1.5 \times 10^{19} \text{ m}^{-3}$. Figure 3(a) indicates that the electron temperature decreases and the ion temperature increases, as the density increases. This dependency can be explained with the

power balance. From Eq. (3), the power balance of electrons and ions are presented with the ohmic power, energy transfer from electrons to ions and heat fluxes in the steady state as

$$\text{Electron} \quad : \quad -\frac{1}{v'} \frac{\partial(v'Q_e)}{\partial\rho} + P_{OH} - P_{EQ} = 0, \quad (9a)$$

$$\text{Ion} \quad : \quad -\frac{1}{v'} \frac{\partial(v'Q_i)}{\partial\rho} + P_{EQ} = 0. \quad (9b)$$

Figure 3(b) shows the values at $\rho = 0.3$, where the temperature gradient is large, for the explanation. A larger density leads increase of electron flux and P_{EQ} , which makes the electron temperature smaller. Equations (7) and (8) give

$$P_{EQ} \propto n^2 T_e^{-1.5} (T_e - T_i). \quad (10)$$

Electron-ion collision is responsible to the energy exchange between electrons and ions, which tends to make difference of the temperature between electrons and ions smaller. Increases of n^2 and $T_e^{-1.5}$ and decrease of $(T_e - T_i)$ determines the magnitude of P_{EQ} , as is indicated with the red dashed line in Fig. 3(b). Therefore, the ion temperature increases, as P_{EQ} increases. In addition, the larger plasma resistivity gives P_{OH} increase. Equations (6), and the spitzer's formula for the resistivity

$$\eta = \frac{m_e}{ne^2\tau_{ei}}, \quad (11)$$

give the following relation

$$P_{OH} \propto T_e^{-1.5} j^2. \quad (12)$$

The deviation from this relation indicated by the green dashed line in Fig. 3(b) comes from density dependence of neoclassical resistivity by NCLASS routine.

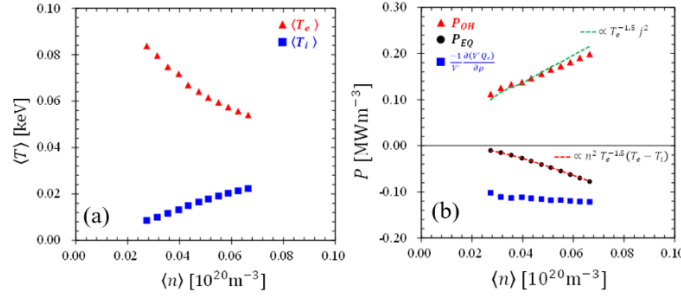


Fig.3. (a) Relationship between volume-averaged temperature and density, when the particle feeding rate is changed. (b) Dependency of terms at $\rho = 0.3$ in the power balance on $\langle n \rangle$.

The other transport analysis is performed with variation of an external coil current. The plasma parameters are same with the previous sections excepts D-coil currents, which are changed in the range from -18.8 to -23.3 kA turn, while the other coil currents are same. The plasma size V_p is changed in accordance with the D-coil current. In the transport model of the TR code, the effect of plasma shape is introduced by the plasma volume, metric $\langle |\nabla\rho| \rangle$ and $\langle |\nabla\rho|^2 \rangle$. As shown in Fig. 4(a), the density slightly decreases with increase of plasma volume. Particle source $S(r)$ decreases as the total particle feeding rate is constant, but the density variation is slight, due to decrease of the particle fluxes.

On the other hand, the larger the plasma shape is, the lower the electron temperature and the higher the ion temperature become. Figure 4(b) shows the values at $\rho = 0.3$ for explanation of the dependency as well. Since the plasma current is kept constant, the current density decreases in accordance with the increase of the plasma volume. Power P_{OH} is represented as

$$P_{OH} \propto T_e^{-1.5} A_p^{-2}, \quad (13)$$

where A_p is the size of the poloidal cross-section of the plasma. Therefore, P_{OH} is decreased depending on A_p as in Fig. 4(b), which gives the decrease of the electron temperature. For the ion temperature, P_{EQ} decreases slightly as A_p increases, but the energy confinement time becomes longer, so the ion temperature increases due to the improvement of confinement.

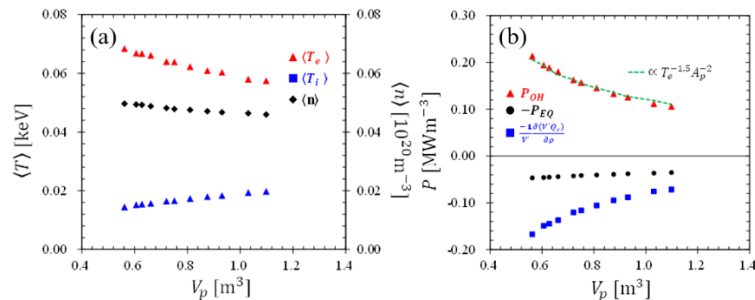


Fig.4. (a) Relationship between volume-averaged density, ion and electron temperature, and the plasma volume. This is the case when I_{D-coil} is changed. (b) Dependency of terms at $\rho = 0.3$ in the power balance on plasma volume.

5. Conclusion

In this study, the transport analyses were performed with calculation of free-boundary condition equilibria, considering external vertical coils in PLATO experiments. The plasma performance was predicted in PLATO. The dependences of plasma performance on the particle feeding rate and vertical field coil current, which are externally controllable parameters in experiments, were evaluated. From these evaluations, it was found that higher density and larger plasma volume give larger ion temperature. Change of energy transfer from electrons to ions, or energy confinement time is the causes for the ion temperature increase. In the initial phase of PLATO experiments, there is no direct ion heating method, so these indirect methods are possible ways to increase the ion temperature. In the present code, toroidal current profiles obtained by transport calculation is not reflected on equilibrium calculation, so the process is necessary to be introduced for self-consistent calculation. In addition, prediction accuracy of transport will be improved by comparing with experimental results in future works.

References

- [1] A. Fujisawa, AIP Conf. Proc. **1993**, 020011 (2018).
- [2] T. Ido, *et al.*, submitted to Rev. Sci. Instrum. (2021).
- [3] M. Honda *et al.*, J. Plasma Fusion Res. SERIES **6**, 160 (2004).
- [4] N. Hayashi and JT-60 Team, Phys. Plasmas **17**, 056112 (2010).
- [5] Y. Murakami *et al.*, J. Nucl. Mater. **313-316**, 1161 (2003).
- [6] <https://bps.nucleng.kyoto-u.ac.jp/task/>
- [7] S. Tomimatsu, *et al.*, Plasma Fusion Res. **15**, 1403052 (2020).
- [8] W. Houlberg, *et al.*, Phys. Plasmas **4**, 3230 (1997).
- [9] M. Yagi *et al.*, Phys. Fluids B **5**, 3702 (1993).
- [10] K. Matsuoka, RIAM Reports, Kyushu Univ. **141**, 51 (2011) (in Japanese).

Effect of Magnetic Fluctuations on the Toroidal Torque Driven by Electron Cyclotron Heating in Tokamak Plasmas

D. Iio, S. Murakami, Y. Yamamoto

Department of Nuclear Engineering, Kyoto University, Nishikyo, Kyoto, 615-8540, Japan

1 Introduction

It is well recognized that toroidal plasma flow and its shear play a significant role in magnetohydrodynamic (MHD) mode stabilization and energy confinement improvement. Particularly, self-generated toroidal flow in Electron Cyclotron Heating (ECH) plasma has been observed and analyzed in many tokamaks, such as JT-60U and DIII-D. The ECH driving mechanism of the spontaneous plasma toroidal flow needs clarifying. Although many experimental studies[1,2] have been done, it has not been completely understood yet.

2 Simulation model

It is known that two toroidal torque components contribute to the plasma toroidal flow, i.e., $j \times B$ torque and collisional torque. The $j \times B$ torque is a consequence of radial ion current in response to the outward flux of energetic electrons with ECH. Collisional friction between energetic electrons and bulk plasma generates the collisional torque. In axisymmetric magnetic field configuration such as ideal tokamak, these two components are of the same magnitude but in different directions, so that total toroidal torque becomes almost zero. However, it is shown that the balance of these two components breaks, and the net torque is generated in non-axisymmetric configuration such as helical devices,[3]. Also, in tokamak devices, it is predicted that the net torque is generated with a small non-axisymmetric component such as toroidal field ripple and resonance magnetic perturbation (RMP).

In this study, we consider the magnetic fluctuations in which toroidal and poloidal modes of several tens are assumed, and investigate the behavior of the energetic electron and the toroidal torque generated by ECH. We use the GNET code, which solves a drift kinetic equation for energetic electrons with ECH in 5D phase space

$$\frac{\partial \delta f}{\partial t} + (\vec{v}_d + \vec{v}_{\parallel}) \cdot \frac{\partial \delta f}{\partial \vec{r}} + \dot{v} \cdot \frac{\partial \delta f}{\partial \vec{v}} - C(\delta f) - L(\delta f) = S^{\text{ql}}(f_{\text{Max}})$$

with the Monte Carlo method[4]. Magnetic fluctuation is considered in the phase of solving the drift equation of motion. We assume that the fluctuation field component $\delta \mathbf{B}$ is perpendicular to the equilibrium field component \mathbf{B}_0 . The fluctuation field is defined as

$$\begin{aligned} \mathbf{B} &= \mathbf{B}_0 + \delta \mathbf{B} \\ \delta \mathbf{B} &= \nabla \times \alpha \mathbf{B}_0, \end{aligned}$$

where α is the function at real space, which describes the shape of the perturbation at the real space. We define the function α as

$$\begin{aligned} \alpha(\psi, \theta, \phi) &= \varepsilon \sum_{mn} b_{mn}(\psi) \cos(m\theta - n\phi + \chi_{mn}) \\ b_{mn}(\psi) &= \exp \left[-\frac{(m - nq(\psi))^2}{4w^2} \right]. \end{aligned}$$

3 Simulation results

We calculate the toroidal torques under the perturbations with the mode numbers of $(m, n) = (10-30, 10)$. In the axisymmetric configuration ($\varepsilon = 0$) these two torques are canceled each other. As seen in the Fig. 1, as the perturbation strength increases, the $j \times B$ becomes dominant and the total torque becomes non-zero. We also calculate the toroidal torques under 2x, 3x and 4x perturbation mode numbers of $(m, n) = (10-30)$. The obtained result is shown in Fig. 2. It is confirmed that as mode numbers increase, the toroidal torques become stronger, especially in the co-direction. According this, it is expected that we can use high mode perturbations for generating toroidal torque instead of strong perturbations. This result indicates the possibility of a significant role on a net toroidal torque generation by high-mode magnetic microturbulence.

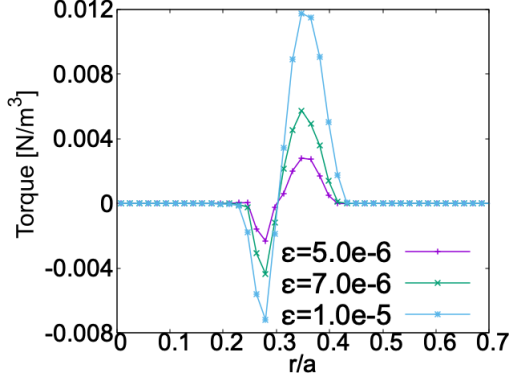


Fig. 1: Total torque at each ε

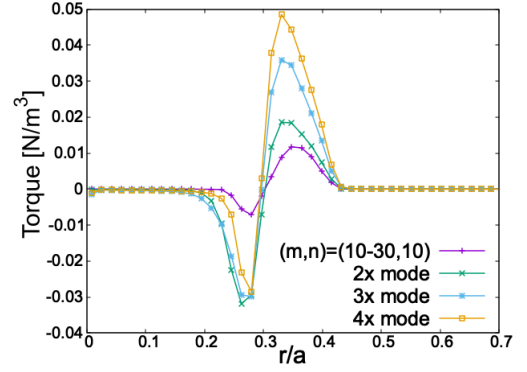


Fig. 2: Total torque at each modes

- [1] M. Yoshida, et al., Phys. Rev. Lett. **103**, 065003 (2009)
- [2] J. S. deGrassie, et al., Phys. Plasmas **11** 4323 (2004)
- [3] Y. Yamamoto, et al., Plasma Fusion Res. **14** 3403105 (2019)
- [4] S. Murakami, et al., Nucl. Fusion **40** 693 (2000)

Magnetic Configuration and Heating Location Dependences of the Toroidal Torques by ECH in LHD

Yasuhiro YAMAMOTO and Sadayoshi MURAKAMI

Department of Nuclear Engineering, Kyoto University, Kyoto, 615-8540, Japan

Toroidal torque by electron cyclotron heating (ECH) is investigated in LHD plasmas, assuming the supra-thermal electrons by ECH generate torques on the plasma through $j_r \times B$ and collisions. The $j_r \times B$ torque depends on the radial drift velocity and the fraction of trapped electrons. Therefore, the magnetic configuration and the heating location affects the toroidal torque. We investigate the magnetic configuration and heating location dependences of the toroidal torques by ECH in LHD, considering typical three magnetic configurations: the inward shifted, standard, and outward shifted configurations. As a result, magnetic ripple bottom heating makes larger torque than that of ripple top heating because of the large fraction of trapped electrons. Also, heating at the outer minor radius makes larger toroidal torque than that of heating at the inner radius, and the injection angle can also change the toroidal torque profile. Moreover, ECH makes the largest toroidal torque in the outward shifted configuration. Finally, With the obtained toroidal torques, we evaluate the toroidal flow velocities with the obtained toroidal torques. We obtained the largest flow near the axis in the standard configuration because of its small viscosity and large toroidal torque.

1 Introduction

Toroidal flow is one of the important issues in turbulence transport and MHD stability. Recently, spontaneous toroidal flows driven by electron cyclotron heating (ECH) have been observed in many tokamaks and helical devices such as JT-60U, LHD, and HSX. Many experimental [1, 2] and theoretical [3] studies have been undertaken to clarify the underlying mechanism. However, the mechanism of the toroidal flow generation by ECH has not yet been understood well.

We previously reported that ECH could apply torques on the plasma through $j_r \times B$ and collisions[6, 7]. Also, the $j_r \times B$ torque overcomes the collisional torque in the non-symmetric configuration. The $j_r \times B$ torque would be a candidate for the torque driving the toroidal flow.

In LHD, toroidal flows have been investigated in the Neutral Beam Injection (NBI) heating and ECH plasmas, where the toroidal flow velocity is measured by the charge exchange recombination spectroscopy (CXRS) [4, 5]. Also, LHD has the flexibility on the magnetic configuration by shifting the magnetic axis. It is known that the confinement of energetic particles of the inward shifted configuration is better than that of the outward shifted configuration due to the trapped particle orbit improvement. Therefore, we expect the $j_r \times B$ torque would be significant in the outward shifted configuration because the radial diffusion of trapped electrons is important for the $j_r \times B$ torque. Also, the heating location varies the fraction of trapped supra-thermal electrons accelerated by ECH. The heating location dependence on the $j_r \times B$ torque would appear through the fraction of trapped electrons. Additionally, including the finite parallel wavenumber, the res-

onance condition is shifted due to the Doppler effect, and the change of the heating source profile in velocity space would appear.

In this study, we investigate the dependences of magnetic configurations and heating location on the toroidal torque by ECH in LHD, applying the GNET code, which can solve a linearized drift kinetic equation for δf electrons by ECH in the 5D phase space[8]. Also, we evaluate the toroidal flow velocities driven by the ECH torques, solving the diffusion equation of toroidal flow.

2 Simulation model

To investigate the electron velocity distribution and the toroidal torque due to ECH, we apply the GNET code, which can solve the drift kinetic equation in 5-D phase space using the Monte Carlo method. We split the gyrophase averaged electron distribution function f into a stationary Maxwellian part f_{Max} and an perturbed part by ECH δf as $f = f_{\text{Max}} + \delta f$. The drift kinetic equation for δf is given by

$$\frac{\partial \delta f}{\partial t} + (\mathbf{v}_d + \mathbf{v}_{\parallel}) \cdot \frac{\partial \delta f}{\partial \mathbf{r}} + \dot{\mathbf{v}} \cdot \frac{\partial \delta f}{\partial \mathbf{v}} - C(\delta f) - L(\delta f) = S^{\text{ql}}(f_{\text{Max}}) \quad (1)$$

where \mathbf{v}_{\parallel} and \mathbf{v}_d are the velocity parallel to the magnetic field and the drift velocity, respectively. Also, $C(\delta f)$, $L(\delta f)$ and $S^{\text{ql}}(f_{\text{Max}})$ are the collision operator, the orbit loss term, and the heating source term of ECH, respectively.

The ECH source term is described by the quasi-linear diffusion theory. We consider only linear effect $S^{\text{ql}}(f_{\text{Max}})$ for simplicity. Then the source term S^{ql} is expressed as

$$S^{\text{ql}}(f_{\text{Max}}) = -\frac{\partial}{\partial v_i} D_{ij}^{\text{ql}} \frac{\partial f_{\text{Max}}}{\partial v_j} \quad (2)$$

where D_{ij}^{ql} is the quasi-linear diffusion tensor and the radial profile of the absorption power density is set as a Gaussian distribution. We consider that the right-handed electric field of the EC wave is dominant for X-mode.

ECH applies torques on the plasma through $j \times B$ and collisions as below. Since the radial movements of trapped electrons accelerated by ECH are faster than those of thermal electrons, ECH can drive the radial electron current j_e . The net current in the steady state should vanish to maintain the quasi-neutrality, so the return current, $j_r (= -j_e)$, must flow in the bulk plasma. Therefore, the bulk plasma feels $j_r \times B$ torque due to the return current. On the other hand, the electrons drift toroidally due to the precession motion. During the slowing down of the energetic electrons, they transfer their momenta to the bulk plasma due to collisions. If we consider the heating source without initial momentum input, the collisional torque of the particles passing in the co-direction should be equal to that of the particles passing in the counter-direction. The trapped particles, however, have precession motion, which can contribute to the net collisional torque. The $j_r \times B$ and collisional torques driven by the heating source without initial momentum input should cancel in the completely symmetric configuration in the symmetry direction except for the effect of the transient orbit width[11, 12]. Therefore, the conservation of angular momentum is satisfied and the total toroidal torque should vanish in the axisymmetric configuration. However, non-symmetric magnetic modes enhance the radial electron flux and break the cancellation of the two torques. Since the $j_r \times B$ torque is dominant in LHD, the ECH torque is subject to the radial drift velocity of trapped electrons and the fraction of trapped electrons.

3 Results

Applying GNET code, we solve the linearized drift kinetic equation for the supra-thermal electrons in 5D phase space and evaluate the deviation of the distribution function from Maxwellian, δf , in the inner shifted ($R_{ax} = 3.6\text{m}$), the standard ($R_{ax} = 3.75\text{m}$) and the outward shifted ($R_{ax} = 3.9\text{m}$) configurations. We assume an ECH plasma with the central electron temperature $T_{e0} = 4\text{keV}$, the central ion temperature $T_{i0} = 1\text{keV}$ and the central electron density $n_{e0} = 1 \times 10^{19}\text{m}^{-3}$. Also, the toroidal magnetic field is $B_t = 1.375\text{T}$.

We investigate the heating location dependence of the total torque, which includes the $j_r \times B$ and collisional torque. The total toroidal torque profiles with different heating location ($r/a = 0.1, 0.3, 0.5, 0.7$, and ripple top ($\theta = 180^\circ, \phi = 0^\circ$) or ripple bottom ($\theta = 0^\circ, \phi = 18^\circ$)) and the integrated toroidal torque for each heating location are shown in Fig. 1. Here, the EC wave is assumed to be injected perpendicularly. Ripple bottom heating makes larger net toroidal torque than top heating because of the fraction of trapped electrons. Also, heating at outer minor

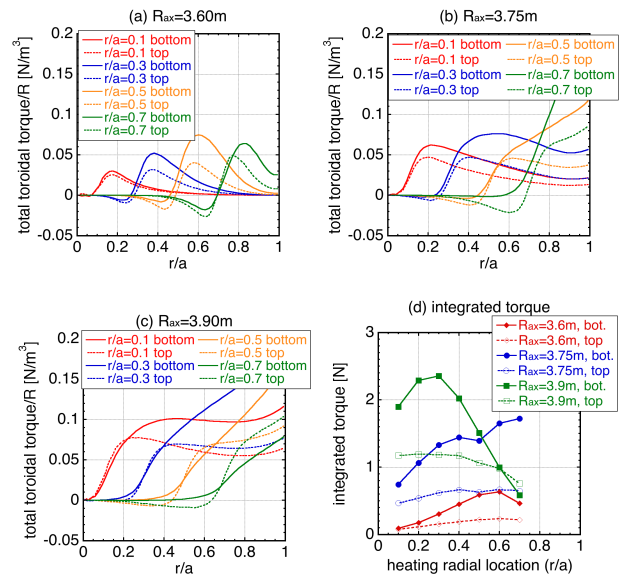


Fig. 1 The toroidal torque profiles with different heating location in (a) the inward shifted configuration, (b) the standard configuration and (c) the outward shifted configuration. Figure (d) shows the dependences of the heating location and the configuration on the integrated ECH torque.

radius makes larger toroidal torque than that by heating at inner minor radius due to the strong magnetic ripple. The integrated toroidal torques by ripple top heating vary moderately with different minor radii of the heating location than those by ripple bottom heating. The difference between the top and bottom heating is comparatively small in the inward shifted configuration. The outward shifted configuration makes larger toroidal torque in the case of heating at inner minor radii because of the worse confinement of supra-thermal electrons. For the outward shifted configuration, however, the integrated toroidal torque of heating at outer minor radii decrease because of the boundary.

We evaluate the toroidal flow $V(r)$ driven by ECH torque, solving the diffusion equation

$$\frac{\partial V(r)}{\partial t} = \frac{1}{r} \frac{\partial}{\partial r} \left(r D \frac{\partial V(r)}{\partial r} \right) + \frac{T(r)}{m_i n_i R} - \mu(r) V(r), \quad (3)$$

where T , D and μ , are the ECH torque, the diffusion coefficient and the viscosity coefficient, respectively. The viscosity coefficient is evaluated as[13]

$$\mu \approx \pi^{1/2} \langle (\hat{\mathbf{n}} \cdot \nabla \mathbf{B})^2 / B^2 \rangle (R/M) (2eT_i/m_i). \quad (4)$$

The viscosity coefficients in the three configurations are shown in the Fig. 2 The obtained toroidal torque is the largest in the outward shifted configuration, while the viscosity coefficient near the axis is the largest in the outward shifted configuration. The outward shifted configuration has the strong driving and damping forces. On the other hand, the inward shifted configuration has the weak driving and damping forces. Their effects conflict. We investigate

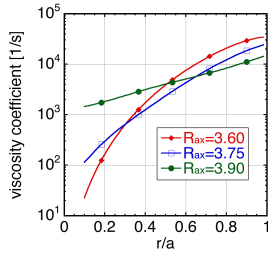


Fig. 2 The neoclassical viscosity coefficients in the three LHD configurations.

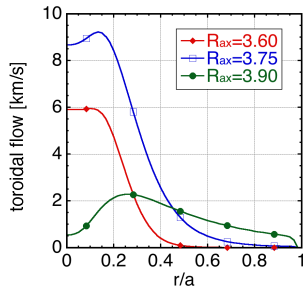


Fig. 3 The toroidal flow velocities obtained by solving the diffusion equation in the three LHD configurations.

the toroidal flows in the three configurations. The steady toroidal flows driven by heating near the axis $r/a \sim 0.1$ are shown in the Fig. 3. As a result, toroidal flow in the standard configuration is the largest with the same input parameter ($D = 1\text{m}^2/\text{s}$, $P = 1\text{MW}$) because of its small viscosity and large toroidal torque. The second largest one is obtained in the inward shifted configuration, which has the smallest viscosity coefficient around the axis in the three configurations.

4 Conclusions

We have evaluated the ECH torque, which consists of the $j_r \times B$ and collisional torques, in LHD plasmas applying the GNET code to investigate the magnetic configuration and heating location dependences of the toroidal torque. In a non-symmetric configuration, the $j_r \times B$ torque can be larger than the collisional torque and generate the net torque. The $j_r \times B$ torque is caused by the radial electron current driven by ECH, which is subject to the radial drift velocity of trapped electrons accelerated by ECH and the fraction of trapped electrons.

Heating at the ripple bottom makes more trapped electrons and thus generates larger toroidal torque than heating at the ripple top. The supra-thermal electrons heated by ECH need pitch angle scattering before they get trapped in the ripple top heating case. Heating at the outer minor radius makes larger torque than heating at the inner minor radius due to the strong magnetic ripple.

The inward shifted configuration has better confinement of supra-thermal electrons than that of the outward shifted configuration. It indicates that the radial velocity of supra-thermal electrons is faster in the outward shifted configuration and generate a larger radial electron current by ECH. Therefore, the outward shifted configuration makes the largest toroidal torque when the ECH heating location is near the axis. When the heating location is set at outer minor radii, the net torque decreases because of the boundary.

Finally, we have evaluated the toroidal flow with obtained toroidal torques, solving the diffusion equation. The driving force, i.e., ECH torque, is the largest in the outward shifted configuration, although the damping force, i.e., the neoclassical viscosity, is the largest in the outward shifted configuration, too. As a result, the obtained toroidal flow is the largest in the standard configuration because of its small viscosity and large toroidal torque. Also, the second largest one is in the inward shifted configuration, which has the smallest viscosity coefficient in the three configurations.

Acknowledgments

The authors thank LHD Experiment Group for their excellent support of this work. This work was supported by JSPS KAKENHI Grant Numbers JP18K03582. This work is also supported by the National Institute for Fusion Science grant administrative budget (NIFS10ULHH021) and the NIFS Collaboration Research program (NIFS19KNST150).

- [1] M. Yoshida, *et al.*, Nucl. Fusion **49**, 115028 (2009)
- [2] S. T. A. Kumar, *et al.*, Nucl. Fusion, **57**, 036030 (2017).
- [3] P. H. Diamond, *et al.*, Nucl. Fusion **53**, 104019 (2013).
- [4] M. Yoshinuma, *et al.*, Fusion Sci. Technol. **58**, 375 (2010).
- [5] K. Ida, S. Kado, and Y. Liang, Rev. Sci. Instrum. **71**, 2360 (2000).
- [6] Y. Yamamoto, *et al.*, Nucl. Fusion (submitted)
- [7] Y. Yamamoto, *et al.*, Plasma Fusion Res. **14**, 3403105 (2019).
- [8] S. Murakami, *et al.*, Nucl. Fusion **40**, 693 (2000).
- [9] M. Romé *et al.*, Plasma Phys. Control. Fusion **39**, 117 (1997).
- [10] S. Hasegawa, *et al.*, Plasma Fusion Res., **8**, 2403083 (2013).
- [11] M. N. Rosebluth and F. L. Hinton, Nucl. Fusion, **36**, 55 (1996).
- [12] A. Snicker, *et al.*, Nucl. Fusion **55**, 063023 (2015).
- [13] K. Ida and N. Nakajima, Phys. Plasmas **4**, 310 (1997).

Coupling of EPED1 model to the integrated model GOTRESS+ and development of JT-60SA operation scenario

M. Honda, N. Aiba, *H. Seto, E. Narita and N. Hayashi

*National Institutes for Quantum and Radiological Science and Technology, Naka,
Ibaraki 311-0193 Japan*

**National Institutes for Quantum and Radiological Science and Technology, Rokkasho,
Aomori 039-3212 Japan*

Extension of the integrated model GOTRESS+

A steady-state transport equation solver, GOTRESS [1,2], has been developed, which benefits from global optimization techniques such as a genetic algorithm and the Nelder-Mead method such that they directly find the solution where a transport flux matches an integrated source. We have developed a novel integrated model GOTRESS+, mainly consisting of the equilibrium and current profile solver ACCOME and the neutral beam (NB) heating code OFMC, other than GOTRESS, for predictions of temperature profiles consistent with an equilibrium and heating profiles. For the development of operation scenarios in JT-60SA and ITER, etc., it is indispensable to predict the pedestal, which accounts for a large proportion of plasma stored energy. In the past GOTRESS+ framework, the pedestal height was artificially given as a boundary condition of the temperatures in GOTRESS. To predict the pedestal width and height in a reasonable fashion, the EPED1 model [3] has been incorporated into GOTRESS+. The EPED1 model is based on the hypothesis that the pedestal is determined by two constraints: the peeling-ballooning stability, and the empirical scaling of the pedestal height observed in DIII-D, the latter of which relies on the kinetic ballooning turbulence theory. Our own EPED1 model works together with ACCOME as an equilibrium solver and the MHD stability code MARG2D [4]. The shapes of the temperature profiles in the edge barrier region by EPED1 are characterized as the hyperbolic tangent ones. Multiple interface programs have been newly developed to join a temperature profile by GOTRESS given at discrete points and that by EPED1 given by the hyperbolic tangent function at the

boundary of GOTRESS simulations. In short, GOTRESS+ is now extended to predict the plasma profiles entirely inside the plasma, provided that the density profiles are given.

Extension of the integrated model GOTRESS+

We demonstrate an operation scenario development with GOTRESS+ for the ITER-like operation scenario in JT-60SA, what is called #4-1: $B_T = 2.28\text{T}$, $I_p = 4.6\text{MA}$ and $P_{NB} = 24\text{MW} + 10\text{MW}$. The 24MW NB heating is delivered by the positive-ion-source NBI and the remaining by the negative-ion-source NBI. The CDBM model is used as the core transport model. As shown in Fig. 1, the temperature profile and the safety factor profile are converging as iteration continues. It can be seen that the temperature profile in the edge barrier region predicted by EPED1 varied for the first two iterations, but was almost unchanged after the third. Followed by the edge temperature profiles, the core temperature profiles are determined subsequently. The plasma finally obtained virtually meets the target values: the normalized beta of 2.71(~ 2.8), the energy confinement improvement of 1.09(~ 1.1), where the values in the brackets correspond to the target ones. The extended GOTRESS+ will be utilized for other scenarios.

References

- [1] M. Honda, Comput. Phys. Commun. **231** (2018) 94.
- [2] M. Honda and E. Narita, Phys. Plasmas **26**, 102307 (2019).
- [3] P. B. Snyder et al., Phys. Plasmas **16**, 056118 (2009).
- [4] N. Aiba et al., Comput. Phys. Commun. **175**, 269 (2006).

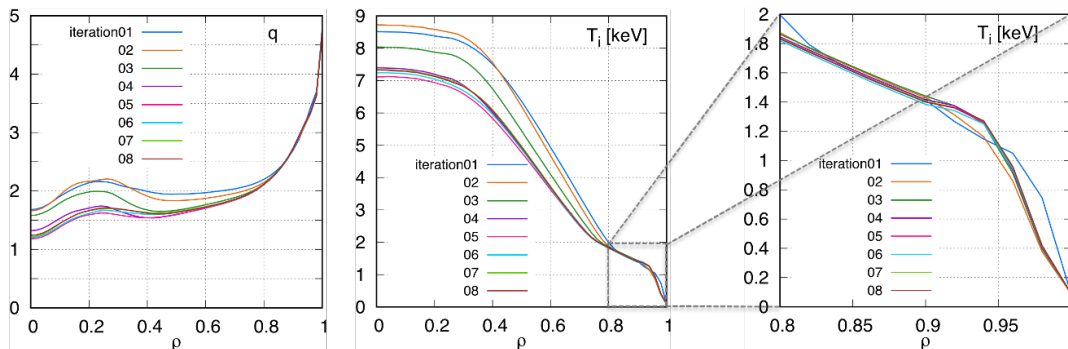


Fig. 1: Predicted profiles of the safety factor and the ion temperature at each iteration by GOTRESS+. The right figure is the close-up of the ion temperature in the edge barrier region.

Extraction of turbulent structures and quantification of energy transfer among structures by singular value decomposition

RIAM Kyushu Univ.^A, RCPT Kyushu Univ.^B, Warwick Univ.^C, NIFS^D,

IGSES Kyushu Univ.^E, CCFE^F, Shimane Univ.^G

M. Sasaki^{A, B, C}, T. Kobayashi^D, Y. Kawachi^E,

R. O. Dendy^{B, C, F}, H. Arakawa^G, S. Inagaki^{A, B}

Magnetically confined plasmas are the typical non-equilibrium open system so that the transport of heat, particles and energy is self-consistently determined by turbulence and its nonlinear structural formations. Dynamical behavior, such as limit cycle oscillation, is observed in cases of zonal flows, toroidal intrinsic rotation, and transport barrier formation, etc [1]. In order to understand such phenomena, it is important to extract spatio-temporal structures with a minimal number of degrees of freedom and to quantify the interaction among them.

In this study, we performed three-dimensional turbulence simulation to demonstrate how to extract the spatio-temporal structures and to quantify the energy transfer among them by using the singular value decomposition. We obtained the cases which corresponds to the Kelvin-Helmholtz turbulence with a dynamical limit cycle oscillation of background plasmas which is accompanied by flow pulsation and avalanche-like transport [2]. The abruptness of flow change contributes to the sustainment of the limit cycle.

The singular value decomposition is applied to spatio-temporal data obtained in the simulation, and the four typical structures are identified from the SVD modes; the background flow deformation, zonal flow, a coherent fluctuation, and intermittent fluctuation. The obtained zonal flow is found to be synchronized with the limit cycle, which determines the frequency of the zonal flow. Next, we formulated the energy of the extracted SVD modes based on Hasegawa-Wakatani model, and evaluated the energy transfer functions by the simulation output. It was clearly shown that the energy transfer characteristics dynamically changes with the limit cycle, and that the nonlinear coupling between the intermittent structure and the coherent mode plays the significant roles for the flow pulsation [3]. The energy flow pattern is summarized in Fig. 1.

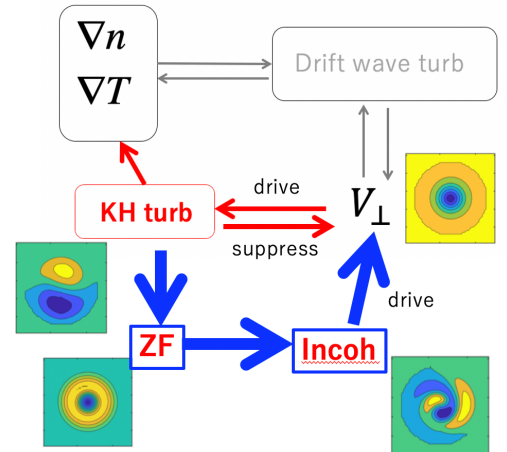


Fig. 1: Energy flow among the

[1] K. Itoh, et. al., **8**, 1102168 (2013).

[2] M. Sasaki, et. al., Phys. Plasmas, **26** 042305 (2019).

[3] M. Sasaki, et. al., Plasma Phys. Control. Fusion, **63**, 025004 (2020).

トカマクプラズマにおける不純物制御のための統合輸送

シミュレーションスキームの開発

Development of Integrated Transport Simulation Scheme for Impurity Control in Tokamak Plasmas

N. Kasuya ^{1,2}, S. Mochinaga ², A. Fukuyama ³, I. Shimomura ², and M. Yagi ⁴

¹ RIAM, Kyushu University, Kasuga, Fukuoka 816-8580, Japan

² IGSES, Kyushu University, Kasuga, Fukuoka 816-8580, Japan

³ Kyoto University, Nishikyo-ku, Kyoto 615-8540, Japan

⁴ QST, Obuchi, Rokkasho, Aomori 039-3212, Japan

E-mail: kasuya@riam.kyushu-u.ac.jp

One of the most important problems in nuclear fusion reactor is control of impurities from the reactor wall, because high z materials are planned to be used for the diverter plates, which has large impact on the confinement of core plasmas. Some experiments show that the radio frequency wave heating, as electron cyclotron heating (ECH) and ion cyclotron heating (ICH), is effective for impurity control in the central region of tokamak [1]. Variation of the background plasma profile is known to affect the neoclassical transport of impurities [2]. In this research, integrated transport simulation code TASK [3] is developed to establish a control scenario of tungsten in the core plasmas.

Transport calculation module for impurities has been newly developed to include neoclassical and turbulent transport processes and atomic processes [4]. The impurity transport module is coupled with the transport module of main plasma components and wave heating module to evaluate response of both main and impurity components to ECH modulation (Fig. 1). Data communication between the modules is implemented using data interface BPSD in TASK for self-consistent calculation.

Transport analyses are carried out using the simulation scheme with plasma parameters on middle size tokamak devices. Figure 2 shows time evolutions of the temperature of deuterium ion and electron, density, power loss, and density of impurity ions. Neoclassical inward pinch in the region with large density gradient of the deuterium ions near the plasma edge induces accumulation of impurities at the center of the plasma. The increase of the impurity density leads increase of the line radiation losses as in Fig. 2(c), which causes decrease of the temperature near the plasma center. Radiation collapse occurs in the larger impurity influx case.

Response of neoclassical transport of impurities is focused on in the central region of tokamaks, where the background pressure profile is not steep. It is demonstrated that radiation collapse can be avoided with additional ECH. The case in Fig. 3 has the large impurity influx enough to induce the radiation collapse, and the 2nd higher harmonic ECH at the center is applied. Increase of the temperature and decrease of the density of the bulk ion by the additional ECH reduce the impurity inward pinch to avoid the radiation collapse. In this way, integrated transport simulation code TASK is developed to establish a control scenario of tungsten in the core plasmas. The simulation with fusion reaction is future task for next generation tokamaks.

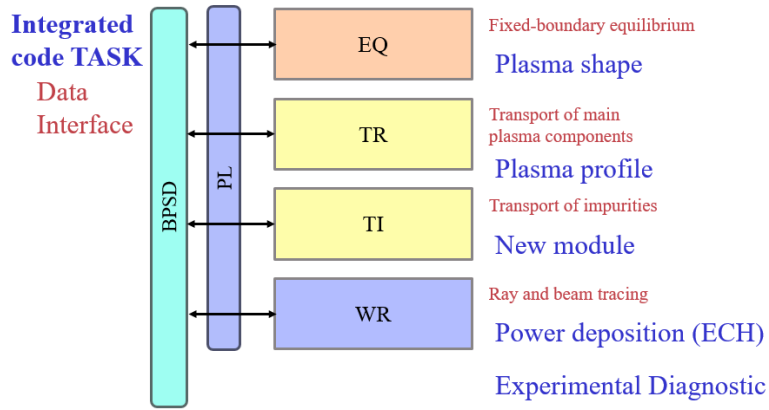


Fig. 1: Schematic of module configuration in TASK integrated simulation code used in this research.

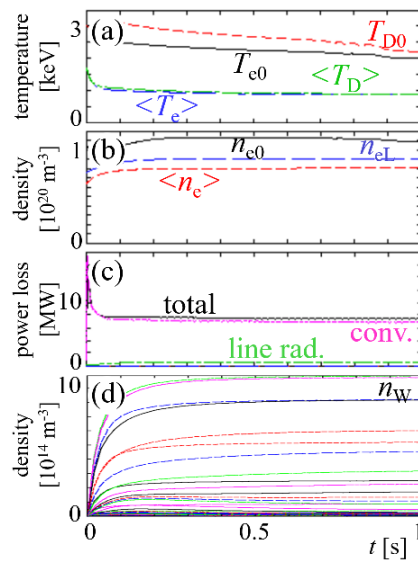


Fig. 2: Time evolutions of (a) temperature of deuterium ion and electron, (b) density, (c) power loss, (d) density of impurity ions. This is the case with ASDEX-U parameters.

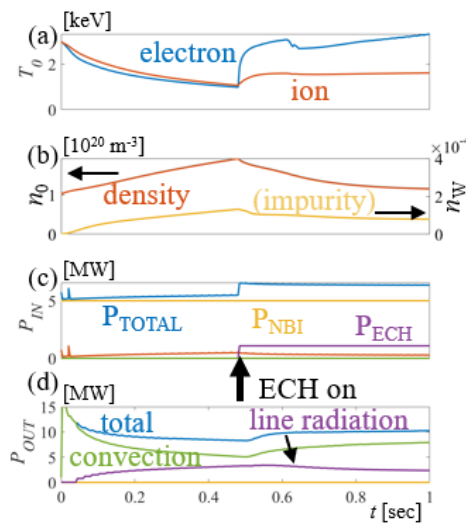


Fig. 3: Time evolution of impurity ions when ECH is applied. (a) Temperature of deuterium ion and electron, (b) density of deuterium ion and impurity ions, (c) input power, (d) loss power are shown. The increase of the impurity density is halted with ECH injection from $t = 0.5$ sec.

Acknowledgements

This work was partly supported by JSPS KAKENHI Grant Number (17H06089, JP20K03905), by the collaboration program of NIFS (NIFS19KNST144) and RIAM of Kyushu University.

References

- [1] R. Neu, *et al.*, Plasma Phys. Control. Fusion **44** (2002) 811.
- [2] C. Angioni, *et al.*, Nucl. Fusion **54** (2014) 083028.
- [3] <https://bpsi.nucleng.kyoto-u.ac.jp/task/>.
- [4] I. Shimomura, *et al.*, 17th BPSI meeting (Fukuoka 2019) 2-6.

Ion mass number dependence of resistive drift wave turbulence

ISHIDA Masanobu¹, KASUYA Naohiro^{1,2}, IMAHASHI Yudai¹, YAGI Masatoshi³

¹IGSES, Kyushu Univ., ²RIAM, Kyushu Univ., ³QST

1. Introduction

Since turbulence structures have great influence on plasma transport, understanding of their formation mechanism is important for the control of fusion plasmas. Experiments in linear device PANTA have shown that there exist several types of nonlinear structures generated by drift wave instabilities, depending on parameters [1], such as streamers [2], zonal flows and solitary drift waves [3]. Numerical simulations also have shown structural bifurcation [4,5]. On the other hand, it is known that the change of ion mass number leads turbulence suppression in fusion plasmas [6]. In this study, we perform numerical simulations for the linear device using turbulence code Numerical Linear Device (NLD) [7]. Difference of nonlinear saturation states of resistive drift wave instability is illuminated with change of discharge gas.

2. Simulation code

The target of this study is the linear device PANTA in Kyushu University, which produces a cylindrical plasma with homogeneous magnetic field in the axial direction. Resistive drift wave instability in PANTA plasmas is calculated using the three-field reduced fluid equations [7]. The set of model equations is solved time evolutions of density N , electrostatic potential ϕ , electron velocity in the magnetic field line direction V for a plasma with a cylindrical shape (Fig. 1). Neutral particles exist even in the center of this rather low temperature plasma, so the effect of neutrals is included by the ion-neutral collision ν_{in} terms. The boundary conditions are given as a periodic boundary in the axial direction, and zero fluctuations at the plasma center and outer boundary in the radial direction. The mean component is also calculated in the nonlinear simulation.

The simulation parameters are the followings; magnetic field $B = 0.1\text{T}$, electron temperature $T_e = 3\text{eV}$, plasma radius $a = 7\text{cm}$, device axial length $\lambda = 4\text{m}$, electron-ion collision frequency $\nu_{ei}/\Omega_{ic} = 300$, electron-neutral collision frequency $\nu_{en}/\Omega_{ic} = 10$. The value of ν_{in} is evaluated depending on the ion species.

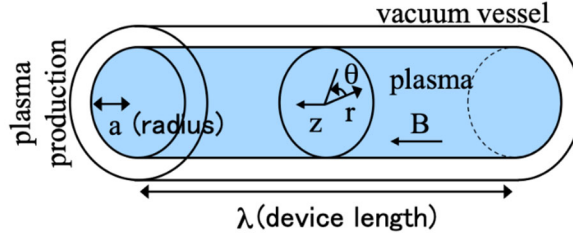


Fig. 1 Schematic of linear device plasma

3. Simulation results

First, a linear analysis of eigen modes is performed. The model equations are linearized, and the radial mode structure and the eigen values are calculated for each mode with azimuthal mode number m and axial mode number n . Using the PANTA device parameters, the cases with discharge gas argon (Ar), neon (Ne), and helium (He) are analyzed. A fixed background density profile is used. Linear growth rate dependence for Ar, Ne and He with the same collision frequency $\nu_{in} = 0.05$ shows that there are unstable modes in the range of $m < 10$ and $n < 3$. In the He case, the linear growth rates in the wide (m, n) region increases (the region with growth rate > -0.01 is wider), but most of them are less than zero. The maximum of the growth rate for He is also smaller than the cases for Ar and Ne. Actually, the collision frequencies are different for different ion species. By considering the effective radius of atoms, ν_{in} of He is smaller than those of Ne and Ar. Figure 2 show the linear growth rate dependence with consideration of the ν_{in} value. The unstable modes exist in the wider range in the He case. This is due to the difference in the normalized distance. The distance is normalized by effective Larmor radius $\rho_s = \sqrt{MT_e/eB}$ evaluated by using the electron temperature T_e in this model, which depends on the ion mass M . The longer normalized distance, even with the same plasma radius, enables modes with larger mode number m and n to be unstable in the He case.

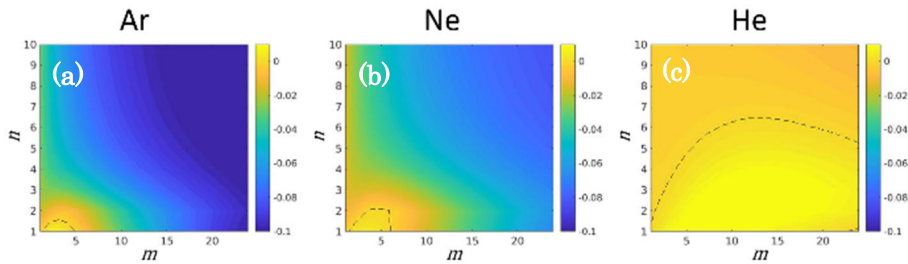


Fig. 2 m and n dependence of the linear growth rate for (a) Ar ($\nu_{in} = 0.1$), (b) Ne ($\nu_{in} = 0.08$) and (c) He ($\nu_{in} = 0.01$). The dotted line indicates the unstable boundary with zero growth rate.

Next, nonlinear calculations are performed for resistive drift wave turbulence. Figure 3 shows the time evolution of mode energy in the case of Ar with $\nu_{in} = 0.1$. In the linear phase, modes with $(m, n) = (2, 1)$ and $(3, 1)$ become unstable in the linear phase, and are still dominant in the nonlinear phase.

Those higher harmonics are also excited, but the limited number of modes are dominant to form a streamer. On the other hand, in the He case with $\nu_{in}=0.01$, the modes around $(m, n) = (7, 4)$ are excited (Fig. 4(a)), and their mode couplings give the nonlinear saturation (Fig. 4(b)). The energy of the unstable modes is transferred to the other modes, and a wide range of modes have the same level of amplitudes, resulting a turbulent state (Fig. 4(c)). A zonal flow with $(m, n) = (0, 0)$ is also excited. The linear analysis as in Fig. 2 predicts that the number of unstable modes is larger in the He case. The difference in the linear mode spectra gives the difference in the nonlinear saturation states (zonal flow or streamer states) by changing the number of unstable modes.

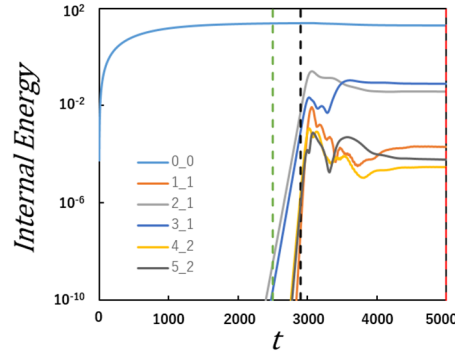


Fig. 3 Time evolution of internal energy of each mode. The cases of Ar with $\nu_{in} = 0.1$ are shown. The $(m, n) = (0, 0)$ component indicates the evolution of the background plasma density.

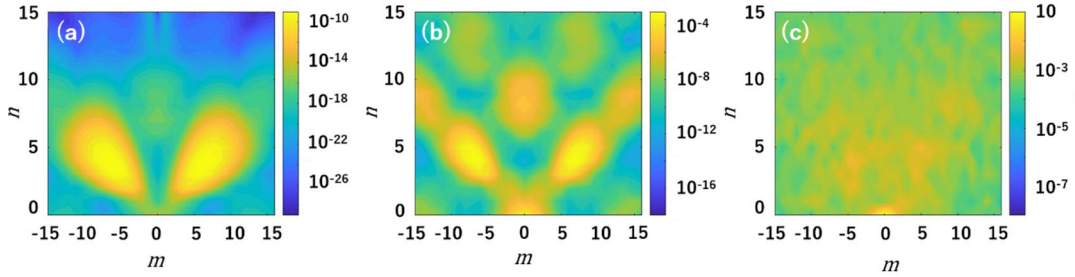


Fig. 4 Mode spectra in (a) linear, (b) developing from linear to nonlinear and (c) nonlinear phase of the He case.

4. Conclusion

The ion mass dependence of the resistive drift wave instability, which is the driving source of turbulence, is investigated for the linear device PANTA in the case of Argon, Neon and Helium discharge gases. Nonlinear calculations are performed with the conditions obtained from the linear analysis, and it is shown that the difference of the characteristic length (Larmor radius) causes the difference of the spectra and the turbulent structure in the nonlinear phase. We will investigate the characteristics in mode spectra and turbulent states obtained in this analysis by comparing with experiments.

Acknowledgement

This study is partially supported by the Grant-in-Aid for Scientific Research (JP17H06089, JP20K03905) of JSPS, the collaboration program of NIFS (NIFS19KNST144) and of RIAM of Kyushu University.

References

- [1] T, Kobayashi, *et al.*, Plasma Fusion Res. **12**, 1401019 (2017)
- [2] T. Yamada, *et al.*, Nature Phys. **4**, 721 (2008)
- [3] H. Arakawa, *et al.*, Plasma Phys. Control. Fusion **53**, 115009 (2011)
- [4] N, Kasuya, *et al.*, Phys. Plasmas **15**, 052302 (2008)
- [5] M, Sasaki, *et al.*, Phys. Plasmas **22**, 032315 (2015)
- [6] M, Nakata, *et al.*, Phys. Rev. Lett., **118**, 165002 (2017)
- [7] N, Kasuya, *et al.*, J. Phys. Soc. Jpn. **76**, 044501 (2007)

Effects of Toroidal Field Ripple on Toroidal Torque by Electron Cyclotron Heating in JT-60U Plasma

Hiroki ISHIGURO¹, Sadayoshi MURAKAMI¹, Yasuhiro YAMAMOTO¹, Mitsuru HONDA²

1. Department of Nuclear Engineering, Kyoto University

2. National Institutes for Quantum and Radiological Science and Technology

1 Introduction

In recent years, spontaneous toroidal flow due to electron cyclotron heating (ECH) has been observed in many tokamaks and helical devices such as JT-60U [1], HSX, and LHD. ECH drives the radial electron current \mathbf{j}_e by increasing the radial motion of supra-thermal electrons. In the steady state, the return current \mathbf{j}_r ($= -\mathbf{j}_e$) flows to maintain the quasi-neutrality, and the resulting torque (so-called $\mathbf{J} \times \mathbf{B}$ torque) drives the rotation of the bulk plasma. When the supra-thermal electrons are generated by ECH, a toroidal flow is generated by the precession of the electrons. This toroidal flow of supra-thermal electrons gives momentum to the bulk plasma by friction and the torque is called the collisional torque. In the case of an axisymmetric field, the $\mathbf{J} \times \mathbf{B}$ torque and the collision torque cancel each other out [2].

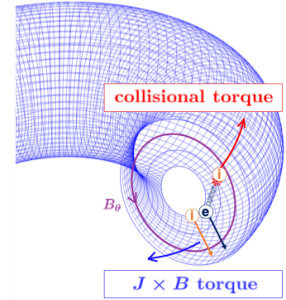


Fig.1: Principle of torque generation

In our previous studies, we have shown that ECH generates toroidal flow in the plasma due to $\mathbf{J} \times \mathbf{B}$ torque and collisional torque in helical plasmas [3]. Although the ideal tokamak is axisymmetric, the magnetic field strength varies in toroidal direction called as “toroidal magnetic ripple” since the system has a finite number of TF coils (JT-60U has 18 TF coils.). In this study, we evaluate the toroidal torque due to ECH by varying the ripple strength using the GNET code. We assume the magnetic configuration of JT-60U and the toroidal field ripple as

$$B = B_{\text{axisym.}} + B_{0,18} \cos(18\phi) \quad \text{where} \quad B_{0,18} = -\delta B_{0,0} \quad (\delta = 0 \text{ to } 0.2 \%). \quad (1)$$

2 Simulation model

In this study, we use the GNET code [4]. GNET code solves the drift kinetic equation Eq. (2) for energetic electrons in 5-D phase space $(r, \theta, \phi, v_{\parallel}, v_{\perp})$ using the Monte Carlo technique.

$$\frac{\partial \delta f}{\partial t} + (\mathbf{v}_d + \mathbf{v}_{\parallel}) \cdot \frac{\partial \delta f}{\partial \mathbf{r}} + \dot{\mathbf{v}} \cdot \frac{\partial \delta f}{\partial \mathbf{v}} - C^{\text{coll}}(\delta f) = S^{\text{ql}}(f_{\text{Maxwell}}) \quad (2)$$

where δf is the displacement of the electron velocity distribution function from the Maxwell distribution due to ECH. For the source term S^{ql} , we use a quasi-linear diffusion term that takes into account the spread in phase space. Since we assume second harmonic X-mode EC waves in this study, we use an approximate expression for second harmonic X-mode for S^{ql} .

$$S^{\text{ql}}(f_{\text{Maxwell}}) = -\frac{D_{ij}^{\text{ql}}}{v_{\text{th}}^2} \left(\frac{v_{\perp}}{v_{\text{th}}} \right)^2 \left[2 - \left(\frac{v_{\perp}}{v_{\text{th}}} \right)^2 - v_{\perp}^2 \frac{\gamma^3}{\Delta c^2} \left(1 - \frac{k_{\parallel} v_{\parallel}}{\omega} \right) X \right] \exp(-X^2) f_{\text{Maxwell}} \quad (3)$$

where $X = [\gamma(1 - k_{\parallel} v_{\parallel} / \omega) - 2\Omega_{ce} / \omega] / \Delta$ and Δ is a very small parameter ($\ll 1$).

3 Result

We have simulated JT-60U with typical plasma parameters. (large radius $R = 3.44\text{m}$, small radius $a = 1.05\text{m}$, magnetic field in magnetic axis $B = 3\text{T}$). Fig.2 show typical trajectories of a trapped electron (initial electron energy is 10 keV). When there is no ripple (left. $\delta = 0.00\%$), the electron drifts along the magnetic surface, but when there is a ripple (right. $\delta = 0.50\%$), the electron moves significantly in the radial direction. Fig.3 shows that as the ripple strength increases, the electron radial flux increases. Fig.4 shows the dependence of the toroidal torque on the ripple strength. The $\mathbf{J} \times \mathbf{B}$ torque increases as the ripple strength increases. This is thought to be due to an increase in the number of particles trapped in the ripple and an increase in the electron radial flux. On the other hand, the collisional torque is almost unchanged. In the case of an axisymmetric magnetic field configuration ($\delta = 0.00\%$), the $\mathbf{J} \times \mathbf{B}$ and collisional torques cancel and no net torque appears. The small amount of torque remaining is due to the finite banana width effect. On the other hand, for the non-axisymmetric field configuration ($\delta > 0.00\%$), a finite torque appears. The toroidal torque of JT-60U obtained with $\delta = 0.0 \sim 0.20\%$ is about $1/10 \sim 1/100$ of the typical torque obtained in a helical magnetic confinement LHD.

Next, we compare the toroidal torque obtained from the simulation with the torque obtained from the theoretical model [5]. Considering that the particles trapped in the ripple drift directly in the radial direction as shown in Fig.2(right), and assuming that the trapped supra-thermal electrons drift only for the time they are trapped, the maximum value of the toroidal torque is given by

$$F_{\max}^{\text{ECH}} \sim \frac{1}{\Delta_{\text{abs}}} \int_0^{\Delta_{\text{abs}}} dl \frac{f_{\text{tr}} P_{\text{ECH}}}{\langle E_{\text{se}} \rangle} p_r(l) = C_1 \frac{\delta^{3/2}}{n} \left[1 - \exp\left(-\frac{C_2 n}{\delta}\right) \right]. \quad (4)$$

where $p_r(l)$ is the probability of existence of energetic electrons in the radial length l , f_{tr} is the fraction of energetic electrons trapped in the ripple, P_{ECH} is the ECH absorption power, and Δ_{abs} is the radial width of the ECH absorption distribution. In this case, $\delta = 0.0 \sim 0.20\%$ around $C_1 \sim 0.25$, $C_2 \sim 1.0$. The toroidal torques obtained by the simulation show a similar trend to the torques obtained by the model.

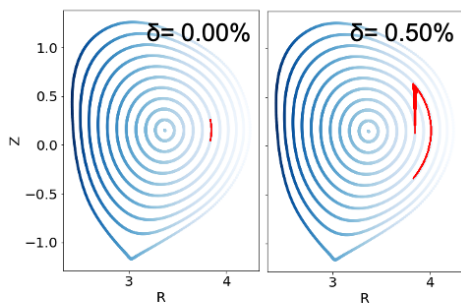


Fig.2: Typical electron orbit
(left)axisymmetric (right)non-axisymmetric

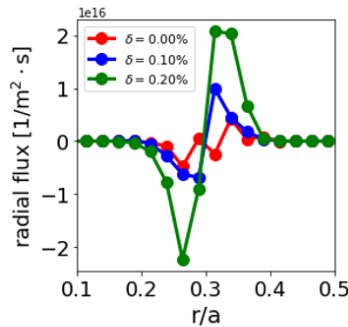


Fig.3: Electron radial flux profile

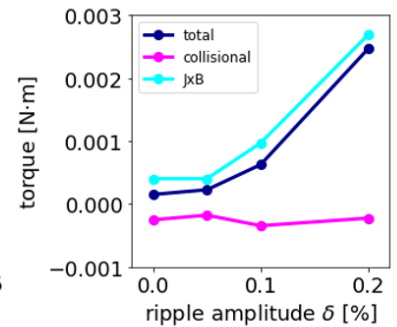


Fig.4: Ripple strength dependence of toroidal torque

- [1] M. Yoshida, et al., Nucl. Fusion **49** (2009) 115028.
- [2] M. N. Rosenbluth and F. L. Hinton, Nucl. Fusion **36** (1996) 55.
- [3] Y. Yamamoto, et al., Plasma Fusion Res. **14** (2019) 3403105
- [4] S. Murakami, et al., Nucl. Fusion **40** (2000) 693.
- [5] S. Murakami, et al., American Physical Society Division of Plasma Physics (2019)

Development of ECCD calculation module for quasioptical ray tracing code

Kota Yanagihara

National Institute for Quantum and Radiological Science and Technology,
Naka, Ibaraki 311-0193 Japan

PARADE (PARaxial RAY DEscription) is newly developed quasioptical ray tracing code, which traces propagation of arbitrary wave beams with refraction, diffraction, polarization, and dissipation in inhomogeneous anisotropic media. In fusion sciences, ray tracing techniques have been used for prediction of electron cyclotron resonance heating and current drive (ECRH/CD). PARADE code can predict ECRH power deposition profile from dissipation calculation with higher accuracy than conventional ray tracing codes, but cannot ECCD for now. Thus, so as to predict the ECCD efficiency profile in tokamak devices, development of ECCD calculation module optimized for PARADE has been started. Adjoint technique, which can estimate the driven RF current with Spitzer function instead of distribution function, has been widely used in many ECRH/CD codes, such as EChamamatsu code. For sufficient result with reasonable calculation time, we also adopted the adjoint technique for our ECCD module. In this paper, predictions performed by PARADE with under-developing new ECCD module are preliminarily compared with the results of conventional EChamamatsu code. Power deposition profiles and driven current profiles by PARADE with ECCD module and EChamamatsu code in JT-60SA plasma (Fig.1) are shown in Figs.2. Toroidal injection angle is fixed to 15° and poloidal injection angle is scanned. Width of each power deposition profiles are similar between both codes. This mean that multi ray imitation of EChamamatsu code is good approximation at least for defocused beam in large JT-60SA plasma with sufficiently low density and magnetic field strength comparing to wave frequency, where diffraction is not crucial. Positions of each power deposition profiles are shifted to inner side for our ECCD code. We expect this might be due to the influence of relativistic effect because PARADE code uses weakly relativistic dispersion tensor for arbitrary wave vector while EChamamatsu code use weakly relativistic tensor for qasi transverse wave vector. The reason of this shift should be cleared as a future work. Driven current profiles are in qualitative agreement but have some differences. Namely, current densities for outside injections with 2nd heating and core injection with 3rd heating of our ECCD module are lower than those performed by EChamamatsu code. This might occur by difference between Spitzer function solvers adopted in our ECCD module and EChamamatsu code. Our module analytically

solves Spitzer function while EChamamatsu code numerically solves it. Influence of this difference for accuracy and computational resources should be studied as a future work.

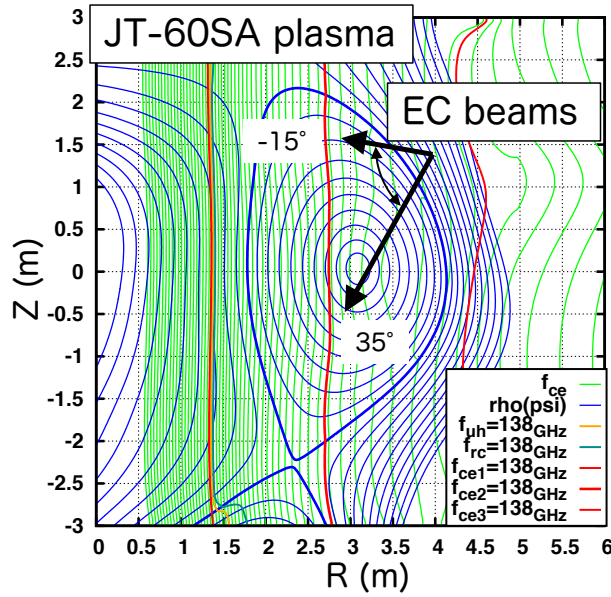
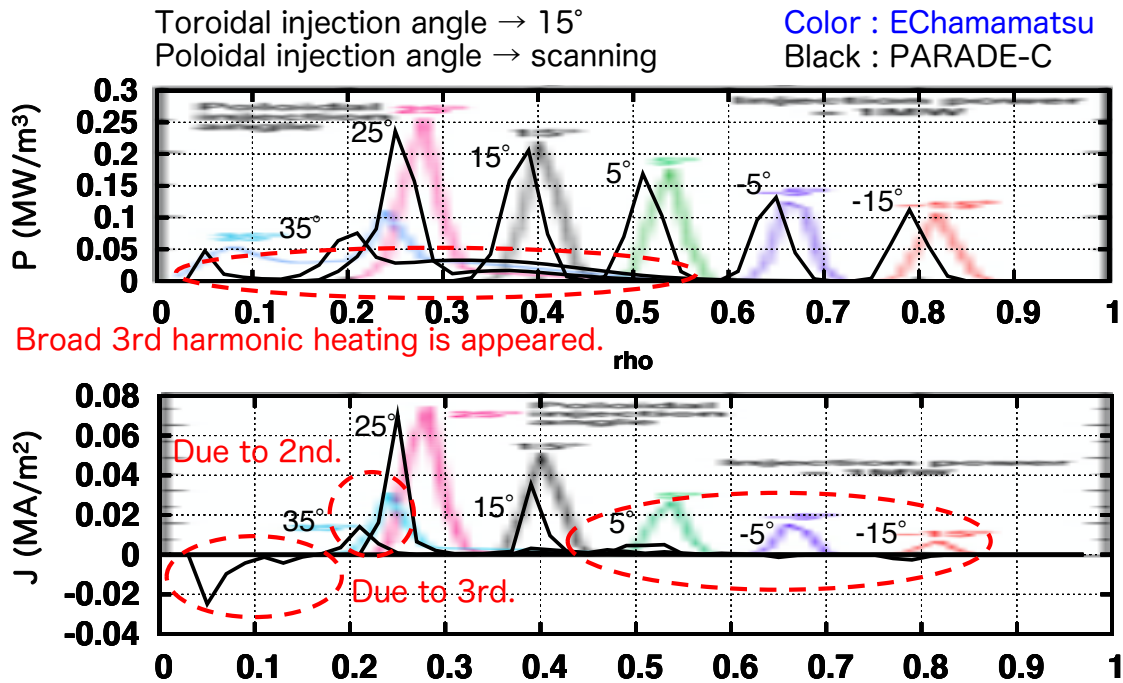


Fig. 1 Poloidal cross section of JT-60SA plasma flux surfaces, magnetic field strength contours, and typical frequencies for 138 GHz EC wave beams, whose poloidal injection angles are schematically indicated with arrows.



Figs. 2 Power deposition profiles and driven current profiles by PARADE with ECCD module (black lines) and EChamamatsu code (colored lines) in JT-60SA plasma shown in Fig.1.

Data assimilation system based on integrated transport simulation applying a reduced model of neutral beam injection heating

Y. Morishita¹, S. Murakami¹, M. Yokoyama^{2,4}, G. Ueno^{3,4,5}

¹*Department of Nuclear Engineering, Kyoto University, Nishikyo, Kyoto, 615-8540, Japan*

²*National Institute for Fusion Science, National Institutes of Natural Science, Toki 509-5292, Japan*

³*The Institute of Statistical Mathematics, Research Organization of Information and Systems, Tokyo 190-8562, Japan*

⁴*The Graduate University for Advanced Studies, SOKENDAI, Toki 509-5292 and Tokyo 190-8562, Japan*

⁵*The Joint Support-Center for Data Science Research, Tokyo 190-0014, Japan*

1. Introduction

Integrated simulation for fusion plasmas has various uncertainties in each of the employed simulation models, specifically turbulent transport model. Because of this, the simulation results also have uncertainties. To solve this problem, we are developing a data assimilation system, ASTI[1], based on the integrated transport simulation code, TASK3D[2].

The purpose of this study is to develop a numerical system that can predict the behavior of fusion plasmas with high accuracy employing the data assimilation. Data assimilation can also improve simulation models involving turbulence models. As data assimilation methods, We use the ensemble Kalman filter (EnKF) to predict the behavior of fusion plasmas with high accuracy and the ensemble Kalman smoother (EnKS) to estimate the models which can reproduce experimental data. To predict the behavior of fusion plasmas in shorter time than real time, it is necessary to reduce the calculation cost of the NBI heating power profile. In this paper, the results of data assimilation applying a reduced NBI heating model are shown.

2. Data assimilation system

In TASK3D, one dimensional (1D) diffusive transport equation is solved. As a turbulent transport model for the LHD plasma, the gyro-Bohm model for electron and the gyro-Bohm gradT model for ion are employed based on previous TASK3D simulations. In the previous study, we employed HREYA and GNET-TD code to evaluate the NBI heating power. However, this calculation takes several hours for a second in actual plasma. To shorten the calculation time to evaluate the NBI heating power, we introduce a reduced model. At the first step of the model, fast ion birth profiles by NBI heating for each beam are evaluated by the interpolation of pre-calculation results of HFREYA and MCNBI code. This interpolation is excited by the Gauss process regression, whose inputs are electron density and temperature profiles. At the second step, the heating power profile are calculated using the simple analytical solution of the Fokker-Planck equation. This calculation takes about a second for a second in actual plasma. We adjust the model parameters (fast ion birth profile, critical velocity, and slowing down time) by the EnKF. Therefore, the state vector is composed of the electron and ion temperature, density, numerical coefficients of turbulent transport models, and the reduced NBI heating model parameters. Every state variable is defined on 60 computational grid points (radial direction, 1-D). The time series data of temperature and density profiles are assimilated into TASK3D.

3. Simulation results

We apply ASTI to a data set simulated by TASK3D using the NBI heating power profiles calculated by HFREYA and GNET-TD base on the LHD shot 114053. Figure 1 shows the assimilation results of T_e and T_i by EnKF, that have been performed with 2000 ensemble members for the cycle of assimilation, $\tau_{DA} = 80$ msec. ASTI can accurately reproduce both the electron and ion temperature in terms of those profiles and temporal variations through the optimization of the employed turbulent transport model and the reduced NBI heating model.

Figure 2 shows the assimilation results of the NBI heating power. The solid lines labeled “Prediction” are the results using the filtered estimate of the reduced NBI heating model parameters, and the dashed lines labeled “TASK3D*” are the results using the smoothed estimates. These results, especially using the smoothed estimates, agree well with the results by HFREYA and GNET-TD (high cost model). It indicates that the reduced NBI heating model supported by data assimilation can reproduce the time-space distribution of NBI heating power calculated by HFREYA and GNET-TD at low calculation cost.

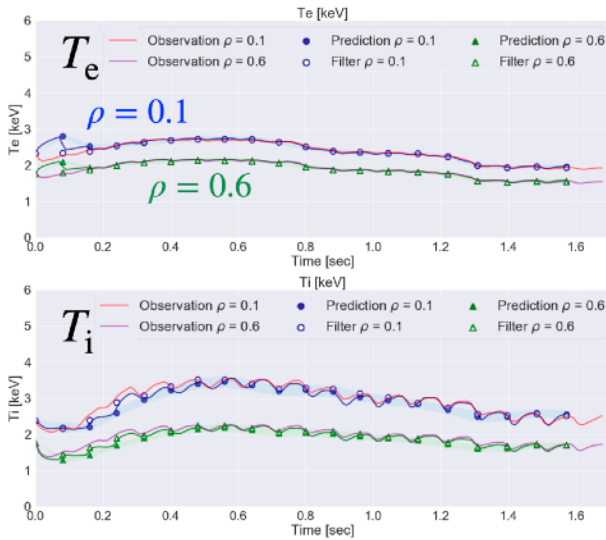


Fig. 1 : Prediction and filtered estimate of temporal change of T_e and T_i for $\rho = 0.0$ and $\rho = 0.6$. Here, ρ is the normalized minor radius.

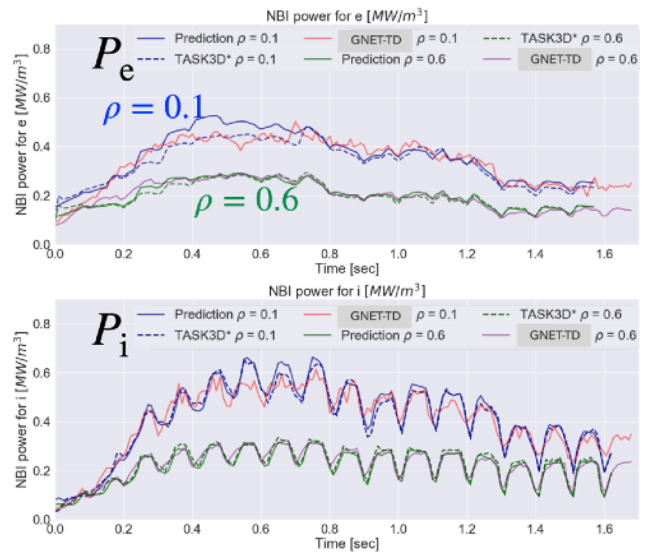


Fig. 2 : Assimilation result of P_e and P_i for $\rho = 0.0$ and $\rho = 0.6$.

4. Summary and future works

We are developing the data assimilation system, ASTI to predict and control the behavior of fusion plasmas in real time. The fast prediction of LHD plasma temperature in a high accuracy has been realized by introducing the reduced NBI heating model into TASK3D and optimizing the model parameters by ASTI. The calculation cost to evaluate the NBI heating power has been reduced from several hours to about a second for a second in actual plasma. To realize the real time prediction, we must speed up the predictive calculation by making the computational grid rougher and the time step longer, and introducing parallel computing into TASK3D.

References

- [1] Y. Morishita, *et al.*, Nuclear Fusion **60**, 056001 (2020).
- [1] S. Murakami, *et al.*, Plasma Phys. Control. Fusion **57**, 119601 (2015).

Evaluation of ballooning and kink instabilities in PLATO tokamak

Y. Kuroda¹, N. Kasuya^{1,2}, M. Sato³, A. Fukuyama⁴, M. Yagi⁵, Y. Nagashima^{1,2}, A. Fujisawa^{1,2}
IGSES, Kyushu Univ.¹, RIAM, Kyushu Univ.², NIFS³, Kyoto Univ.⁴, QST⁵

1. Introduction

Tokamak type device PLATO is under construction in Kyushu university, which enables three dimensional observations of plasma turbulence to improve understanding of plasma instabilities in torus devices [1]. The flexible design of PLATO tokamak makes it possible to observe dynamics of 3-D turbulence structures. Control of Magneto Hydro Dynamics (MHD) instability in tokamak devices is important for stable operation and improvement of confinement performance.

In this study, dynamics of MHD instabilities in PLATO are calculated. The case when ballooning and kink modes both exist is considered, and interaction between them is evaluated by changing the growth rate of the ballooning mode.

2. Equilibrium in PLATO

The expected plasma parameters of PLATO tokamak are the followings; major radius $R = 0.7\text{m}$, minor radius $a = 0.2\text{m}$, plasma volume $V_P = 0.9\text{m}^3$, electron temperature $T_e = 0.2\text{keV}$, density $n = 1.0 \times 10^{19}\text{m}^{-3}$. The plasma equilibria considering the experimental conditions are evaluated by using EQU module in integrated code TASK [2]. TASK/EQU calculates equilibria with the free boundary condition in existence of external vertical coils [3]. Figure 1 shows the example of the obtained magnetic configuration. This calculation gives plasma current $I_p = 40\text{kA}$, ellipticity $\kappa = 1.6$, triangularity $\delta = 0.3$. Previous studies use equilibrium by TASK/EQ, which is the module calculates the magnetic field in the last closed flux surface, for the initial magnetic field distribution of MHD instability calculations [4]. In this study, an interface using TASK/EQU equilibria is developed to introduce the effect of the external coil as an experimental condition.

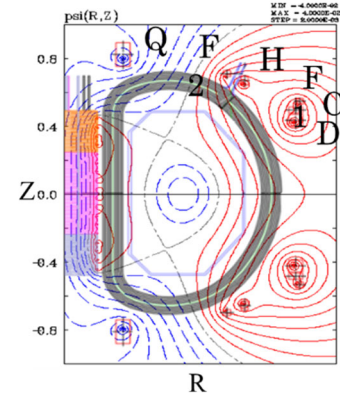


Fig.1 Magnetic configuration obtained by TASK/EQU.

3. MHD simulation

MHD simulations are performed with equilibria obtained by TASK/EQU module as the initial condition. Figure 2 shows the time evolution of the energy with different background pressure gradients. Larger central beta value β_0 gives larger linear growth rate of the ballooning mode, so the increase of the energy is enhanced. The total pressure perturbation energy, which is integrated for the whole plasma volume, increases monotonically in the linear phase, and show nonlinear saturation. Figure 3 shows the time evolution of the

pressure profile. Here, the pressure is normalized by B_0^2/μ_0 . The similar results are obtained for the ballooning and kink mode excitation as in the previous research using TASK/EQ equilibria [4].

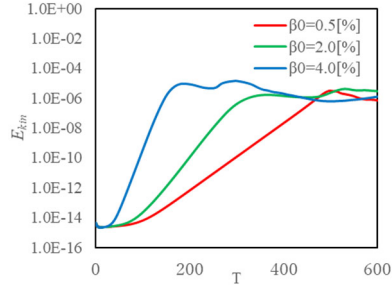


Fig.2 Time evolutions of the total kinetic energy.

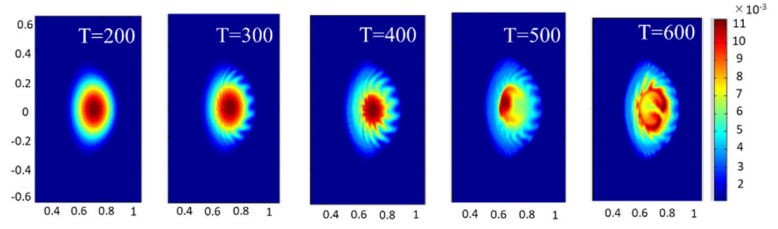


Fig. 3 Time evolution of the pressure profile in the poloidal cross-section with $\beta_0 = 4.0\%$.

4. Characteristic mode structure

In this section the interaction between ballooning and kink modes is investigated by changing the plasma pressure. First, the case when the kink component is dominant for the whole evolution is presented. Here, the $(m = 1, n = 1)$ component and $(m = 14, n = 13)$ component correspond to the kink and dominant ballooning mode, where m and n are the poloidal and toroidal mode numbers, respectively. Figure 4 shows the temporal evolution of the mode structure with $\beta_0 = 0.5\%$. The $(1, 1)$ mode grows around $\rho = 0.3$ in the linear phase. Figure 5 shows the pressure profile at that time. Internal kink mode [5] grows, and the destruction spreads outward. After the spread, various modes are excited nonlinearly near the flux surface with safety factor $q \sim 1$ at $t \sim 500$. Then at $t \sim 550$ the $(1, 1)$ mode grows again around $\rho = 0.3$. This repetitive excitation of the kink mode is observed. The influence of the ballooning components is rather small in this case.

Next, the case when the ballooning component is dominant is presented. Here, the $(m = 1, n = 1)$ component and $(m = 13, n = 12)$ component correspond to the kink and dominant ballooning mode, respectively. Figure 6 shows the temporal evolution of the mode structure with $\beta_0 = 4.0\%$. In Fig. 6(a) the kink mode structure can be seen around $\rho = 0.3$, as in the case with $\beta_0 = 0.5\%$. However, as in Fig. 7, which shows the pressure profile at $t = 200$, the characteristic structure of the ballooning mode can be seen. The linear growth rate of the ballooning mode is increase due to the larger pressure gradient. The $(13, 12)$ component grows near the flux surface with $q = 13/12$ at $t = 200$ as in Fig. 6(b), and nonlinear couplings among several modes induce the $(1, 1)$ component at this region, connected to the kink mode excited at the inner part of the plasma. Then, the mode amplitude becomes smaller after $t = 270$ as the pressure profile is flattened.

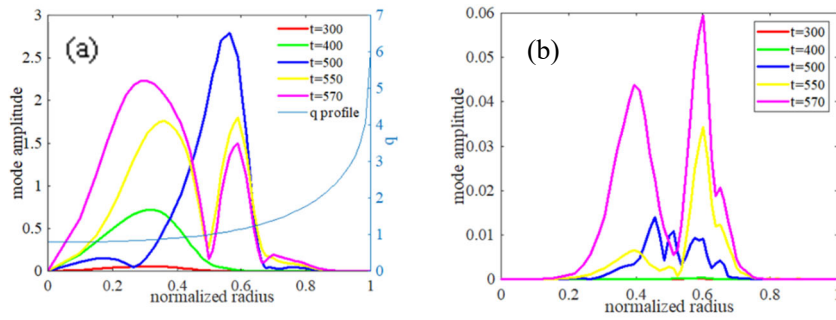


Fig.4 Time evolutions of the mode structures with $\beta_0 = 0.5\%$. The (a) ballooning ($m = 1, n = 1$) and (b) kink ($m = 14, n = 13$) components are shown.

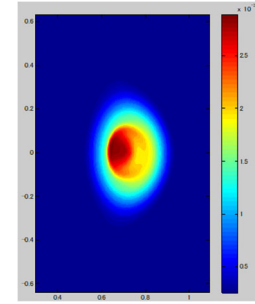


Fig.5 Pressure profile at $t = 400$ with $\beta_0 = 0.5\%$.

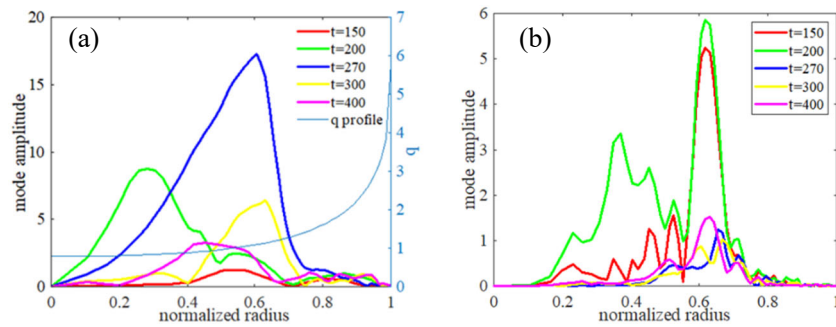


Fig.6 Time evolutions of the mode structures with $\beta_0 = 4.0\%$. The (a) ballooning ($m = 1, n = 1$) and (b) kink ($m = 13, n = 12$) components are shown.

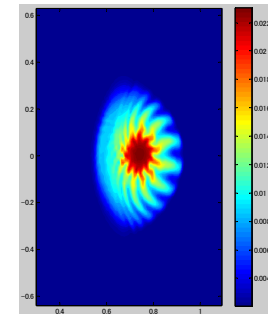


Fig.7 Pressure profile at $t = 200$ with $\beta_0 = 4.0\%$.

5. Conclusion and future plan

In this study, time evolutions in energy and perturbation amplitudes were evaluated by changing the pressure gradient when both ballooning and kink modes are excited. There is difference in the evolution of the radial structure of the $n = 1$ component, and the magnitude of internal collapse is reduced. The observed difference in the growth of the ($m = 1, n = 1$) component is due to the nonlinear interaction between the ballooning and kink modes. In future we will investigate the unstable condition in PLATO by evaluating the dependence of MHD instabilities on the pressure gradient and magnetic shear, and compare it with experiments.

References

- [1] A. Fujisawa, AIP Conf. Proc. **1993** (2018) 020011.
- [2] <http://bpsi.nucleng.kyoto-u.ac.jp/task/>
- [3] K. Matsuoka, RIAM Reports, Kyushu Univ. **141** (2011) 51 (in Japanese).
- [4] S. Tomimatsu, *et al.*, Plasma Fusion Res. **15** (2020) 1403052.
- [5] T. Tsunematsu, Fusion Res. **51** (1984) 101 (in Japanese).